Accepted version: S. Utada, et al., Acta Mater., 121448, 2025. https://doi.org/10.1016/j.actamat.2025.121448

Origin of localizing creep damage in Ni-based single crystal superalloys pre-strained at room temperature

Satoshi Utada[a,b,c,d,1], Milan Heczko[e,f], Jérémy Rame[b,g], Sarah Hamadi[b], Antonín Dlouhý[f], Tomáš Kruml[f], Patrick Villechaise[a], Roger C. Reed[c], Michael J. Mills[e], Jonathan Cormier[a,1]

[a] Institut Pprime, UPR CNRS 3346, Physics and Mechanics of Materials Department, ISAE-ENSMA, BP 40109, 86961, Futuroscope-Chasseneuil Cedex, France

[b] Safran Aircraft Engines, Site de Gennevilliers, 171 boulevard de Valmy—BP 31, 92702 Colombes Cedex, France

[c] Department of Materials, University of Oxford, Parks Road, Oxford, OX1 3PH, United Kingdom

[d] Research Center for Structural Materials, National Institute for Materials Science, 1-2-1 Sengen, Tsukuba, 305-0047, Japan

[e] Center for Electron Microscopy and Analysis, The Ohio State University, 1305 Kinnear Rd., Suite 100, Columbus, OH, 43212, USA

[f] Institute of Physics of Materials, Czech Academy of Sciences, Žižkova 22, Brno, 61600, Czech Republic

[g] NAAREA, Allée de Corse, 92016, Nanterre, 92702 Colombes Cedex, France

KEYWORDS: Ni-based single crystal superalloy; pre-strain; heat treatment; dislocation; creep; microstructure evolution

ABSTRACT

This work investigates mechanisms of irregular microstructure evolution and creep damage localization induced by the prior room-temperature plastic deformation applied to Ni-based single crystal superalloys, AM1 and CMSX-4 Plus, in between solution and aging treatments. Dislocation climb similar to that occurs during the high-temperature low-stress creep is the main mechanism of the microstructure evolution occurring around pre-deformation slip bands, and subsequently leading to the formation of the bands with coarsened γ/γ′ microstructure. Presence of "ready-to-shear" dislocations inside the coarsened γ′ phase is confirmed by a stereo-pair anaglyph of scanning transmission electron microscopy. This native dislocation structure before the high-temperature/low-stress creep test is the origin of creep damage localization observed for the pre-deformed specimens. The comparison of two alloys revealed that magnitude of plastic

---

[1] Corresponding authors: satoshi.utada@nims.go.jp and jonathan.cormier@ensma.fr

activity (precipitation coarsening and dislocation development) inside the bands with the coarsened microstructure is notably larger for AM1 what consequently explains the creep properties degradation under all creep conditions.

1. INTRODUCTION

Ni-based single crystal (SX) superalloys are commonly used for turbine blades and vanes of aero-engine and power generation gas turbines owing to their excellent high-temperature durability and environmental resistance [1–3]. Microstructure of Ni-based superalloy generally consists of a combination of disordered solid solution strengthened face-centered cubic (FCC) γ-matrix and ordered $L1_2$ intermetallic precipitation hardening γ′-precipitates that gives strong deformation resistance at high-temperatures. In order to achieve optimal γ/γ′ microstructure having cubic γ′-precipitates with an average edge length of nearly 0.4-0.5 μm and γ′ volume fraction of 60-70%, solution heat treatment (HT) and one or more aging HTs are applied to the Ni-based SX superalloy components during manufacturing process. This enables the materials to have the best creep resistance at elevated temperatures [4–6].

In reality, arranging microstructure of Ni-based SX superalloy components to perfectly homogeneous with optimal precipitate shape and size is not easy due to the complex turbine blade geometry. This often leads to local unintentional plastic deformation (PD) during production processes such as casting and heat treatments [7,8]. The effects of pre-straining have been studied mainly in two industrial relevant situations: Pre-straining of as-cast (before solution HT) material and after full HT. The first case intends to understand the effect of pre-strain on the recrystallization mechanisms during solution HT. In this scenario, PD can be introduced at temperatures ranging between room temperature (RT) up to supersolvus temperature by tensile, compression, indentation, and grit-blasting to mimic thermomechanical plastic strains introduced during solidification and demolding processes [9–15]. The second case, pre-straining after full HT, usually simulates complex operating conditions of the components. The pre-strain by creep, for example, can generate damaged microstructure that can alter the materials performance of subsequent mechanical tests [16–20].

Few studies focused on the effect of HT process subsequent to unintentional PD of Ni-based SX superalloy component that occurs during production, which can assist an unexpected microstructure evolution around a slip band [8,21–24]. Introduction of tensile PD at room-temperature (RT) induces microstructure evolution similar to the γ′-rafting during HT in order to reduce internal elastic strain around the slip [21,22]. Such microstructure evolution around the former planar slip band leads to the formation of a band with coarsened microstructure, which is described as a “microstructure coarsened band” in our previous works[25,26].

When it comes to the industrial manufacturing of SX turbine blades, special attention needs to be paid for plastic straining during cooling from solution HT temperature [7,8]. This particular case was well simulated by introducing RT pre-deformation between solution and aging HTs of AM1 Ni-based SX superalloy [25,26]. As a consequence of pre-deformation and microstructure evolution that forms the microstructure coarsened band during following HTs, creep properties of the alloy decreased for all creep conditions as summarized in **Table 1**. The fracture planes of pre-deformed specimens were associated with {111} type of crystallographic planes, which are the same type of planes on which the microstructure coarsened bands are located. Recrystallization was triggered inside the microstructure coarsened band during high temperature creep conditions (> 950 °C) that led to early creep rupture with lower rupture strain [25]. Inside the microstructure coarsened bands, faster creep damage accumulation was observed regardless of creep conditions (850 °C / 500 MPa, 950 °C / 300 MPa, and 1050 °C / 140 MPa) [26,27]. Pronounced γ′-raft coarsening, microstructure shearing, and dislocations entering γ′ phase are characteristics of locally accelerated creep in the microstructure coarsened bands. Because creep damage accumulation is locally accelerated within the band and in its neighborhood, the magnitude of prior PD does not affect the subsequent creep life and it appears that the activation of a few slip bands during pre-deformation is enough to trigger the fatal creep life reduction.

With more emphasis on high-temperature low-stress creep condition that triggered recrystallization at the microstructure coarsened band, early creep failure processes with reduced ductility elucidated in the previous studies were illustrated in **Fig. 1** [9,10]. Coarsened and inclined γ′-raft favors dislocations penetrating into γ′ phase that accelerates creep damaging locally, leading to faster creep pores development at the bands [26]. Such creep pores (so-called deformation pores or D-pores [28,29]) already formed before the creep test. To be more specific, D-pores formed during the first stage of aging HT between 1100-1165 °C. Stress concentration and damage accumulation around the D-pores trigger recrystallization and initiate crack along the band, leading to a planar failure with very low rupture strain. These observations were performed using conventional scanning electron microscopy (SEM) combined with electron back scattered diffraction (EBSD). On the other hand, the mechanisms of pore formation and faster and inclined γ′-raft coarsening have not been confirmed with evidence.

Table 1. Summary of creep experiments on pre-deformed AM1 Ni-based SX superalloy [26,27]

AM1	850 °C / 500 MPa		950 °C / 300 MPa		1050 °C / 140 MPa	
	Rupture life (h)	Strain at rupture (%)	Rupture life (h)	Strain at rupture (%)	Rupture life (h)	Strain at rupture (%)
Reference	285.6	21.4	138.7	19.5	417.4	13.9
Pre-deformed	161.4	7.14	102.8	7.7	127.6	2.9

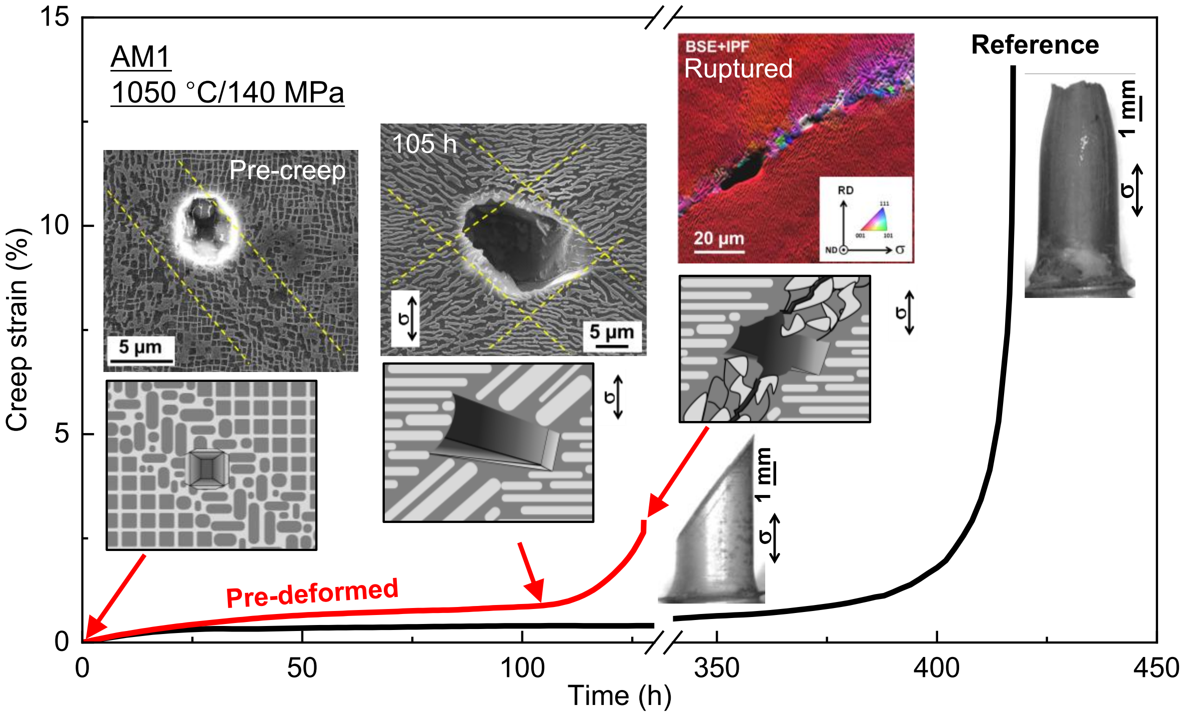

Figure 1. Summary of creep failure processes of AM1 Ni-based SX superalloy with pre-deformation from the previous studies [25,26].

CMSX-4 Plus alloy, having a higher temperature capability compared to AM1 alloy [27,30–32], also showed decreased creep life at 1150 °C / 110 MPa after pre-deformation that seemed similar to AM1 at 1050 °C / 140 MPa [27]. However, pre-deformation did not show strong impact on the creep life and ductility at 1050 °C / 200 MPa [27]. The reasons behind such discrepancy between AM1 and CMSX-4 Plus also remained as an open question from our previous works.

Within this context, this study aims to discuss the effect of prior PD between solution and aging HTs particularly on the defect and dislocation structures and the evolution mechanism during the formation of microstructure coarsened bands. By bridging the mechanisms between the formation of microstructure coarsened band and the development of coarse and inclined γ'-raft structure, the origins of creep damage localization observed during the creep tests of pre-deformed Ni-based SX superalloys are identified. Moreover, pre-deformation mechanisms and the dislocation structure evolution between two tested materials, AM1 and CMSX-4 Plus Ni-based SX superalloys, are compared and discussed in order to understand differences of creep behaviors reported in the previous studies. The discovery in the present work potentially creates critical consequences for the aerospace industry as one might have to consider the impact of pre-deformation on Ni-based SX superalloys' mechanical performance much more seriously.

2. EXPERIMENTAL DETAILS

2.1.Materials and pre-deformation

Two Ni-based SX superalloys, 1st generation AM1 and 3rd generation CMSX-4 Plus, were selected for this study. Nominal compositions of experimental alloys are listed in **Table 2**. AM1 SX bars having a 14 mm diameter were produced by Bridgman directionally solidifying precision casting and they were solution heat treated at 1300 °C for 3 h and cooled down at 5 K/s (300 K/min) in Safran Aircraft Engines foundry. As-cast CMSX-4 Plus SX plate having a 10 mm thickness was produced by the same Bridgman casting and supplied by Safran Tech. Stepwise solution heat treatment (1313 °C / 2 h → 1318 °C / 2 h → 1324 °C / 6 h → 1335 °C / 6 h / air quench (AQ), heating rate between steps was at 1 K/min) for CMSX-4 Plus was performed in Institut Pprime using a conventional resistive furnace. Cooling rate for AQ down to 600 °C is above 5 K/s (300 K/min) at the sample surface. Micrographs of as-solutioned and standard heat-treated materials are shown in **Fig. 2**.

Table 2. Chemical composition of alloys in weight % (Ni bal.).

Alloy	Cr	Co	W	Mo	Ta	Al	Ti	Hf	Re
AM1 [33,34]	7.6	6.7	5.6	2	8	5.2	1.2	0.05	-
CMSX-4 Plus [30]	3.5	10	6	0.6	8	5.7	0.85	0.1	4.8

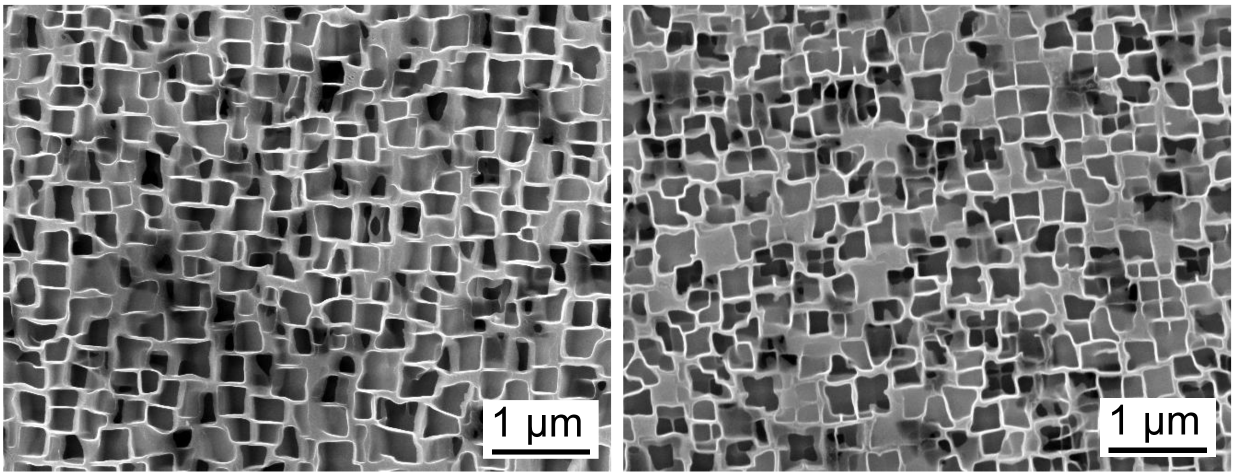

(a) As-solutioned AM1 (1300 °C)　(b) As-solutioned CMSX-4 Plus (1335 °C)

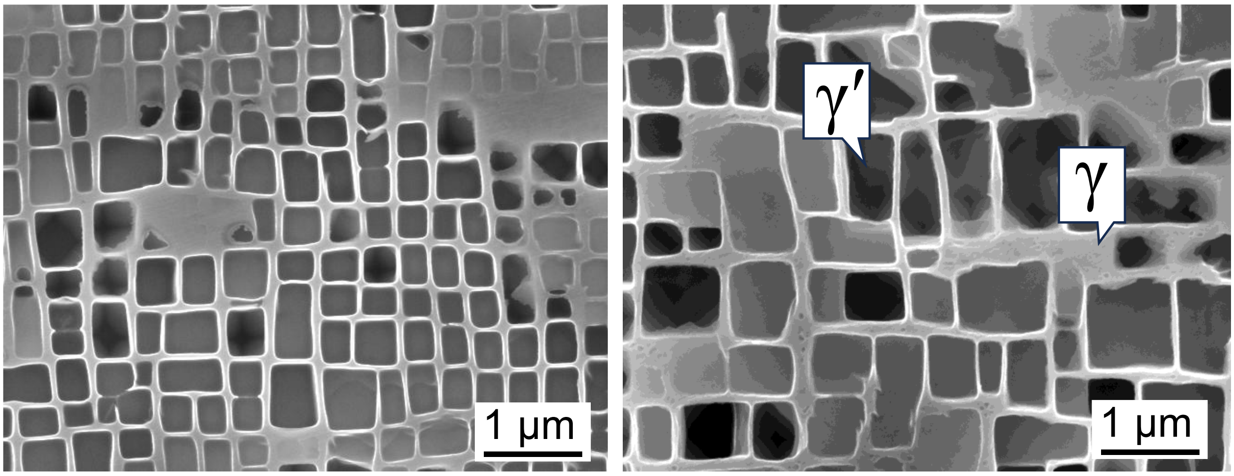

(c) Standard AM1 (solution + 1100 °C / 5 h + 870 °C / 16 h)　(d) Standard CMSX-4 Plus (solution + 1165 °C / 6 h + 870 °C / 20 h)

Figure 2. As-solutioned (a, b) and standard (c, d) microstructures of experimental materials AM1 (a, c) and CMSX-4 Plus (b, d).

A tensile PD was performed at RT with a strain rate of 5×10^{-4} s^{-1} to target approximately 0.8% plastic strain introduced to specimens so that it mimics the plastic deformation during the processing of a turbine blade [8,26]. This process has been used to reproduce microstructures found in the nonconforming turbine blade components from Safran Aircraft Engines foundry [25,26]. Similar microstructural features were also reported in the components from Rolls-Royce as well [8]. SX materials were first machined into rods so that specimens will have crystallographic misorientation from <001> within a 10° tolerance. The rods were then machined into tensile testing specimens having a 14 mm gauge length and a 4 mm diameter (geometry available in reference [35]). This plastic PD, introduced after the solution heat treatment for most of the specimens, was performed using an electromechanical Instron 8562 machine and a contact extensometer. It is noted that under available experimental conditions, it was not possible to control directly the plastic strain, and therefore finally achieved values of plastic strain were slightly below 0.8%. One fully heat-treated AM1 sample was also deformed similarly at RT. The cylindrical surface of a sample after PD was observed using an optical microscope before HTs. Depending on observation purposes, up to two stages of aging HTs were carried out to a pre-strained specimen in a resistive furnace, as listed in **Table 3**. Additionally, prolonged aging treatment at 1050 °C for 500 h was applied (AM1-PD-A1A2A3) to observe the evolution of the microstructure coarsened bands without external load, allowing to identify the effect of pre-deformation and developed dislocations.

Table 3. Preparation history of specimens with a pre-deformation.

Alloy	Specimen designation	Material history
AM1 (As-solutioned)	AM1-PD	PD at RT
	AM1-PD-A1	PD at RT → 1100 °C / 5 h / AQ
	AM1-PD-A1A2	PD at RT → 1100 °C / 5 h / AQ → 870 °C / 16 h / AQ
	AM1-HT-PD-A1	1100 °C / 5 h / AQ → 870 °C / 16 h / AQ → PD at RT → 1100 °C / 5 h / AQ
	AM1-PD-A1A2A3	PD at RT → 1100 °C / 5 h / AQ → 870 °C / 16 h / AQ → 1050 °C / 500 h / AQ
CMSX-4 Plus (As-solutioned)	4P-PD-A1	PD at RT → 1165 °C / 6 h / AQ
	4P-PD-A1A2	PD at RT → 1165 °C / 6 h / AQ → 870 °C / 20 h / AQ

2.2.Scanning electron microscopy

Heat treated specimens were cut along the longitudinal direction close to (100) crystallographic plane and mounted into a conductive resin for precipitate-scale microstructure characterization. Mounted specimens were mechanically polished and finished using 1-μm diamond powder spray and then chemically etched using aqua regia for 8-10 s at around 4 °C to reveal their γ/γ′ microstructure. A JEOL JSM-7000F field emission gun scanning electron microscope (FEG-SEM) was operated to obtain micrographs for γ′ precipitate size analysis. Micrographs containing at least 100 distinguishable γ′ precipitates were used for image analysis by the rotational intercept method (RIM) using in-house RIM-X software (developed by Caccuri et al. [36,37]) to quantify the precipitate evolution morphologies. Precipitates in both outside and inside the microstructure coarsened band were analyzed separately for a comparison.

In our previous study [27], creep tests were performed on pre-strained CMSX-4 Plus at 1150 °C / 110 MPa and drastic creep life reduction (126 h → 25 h) was observed as described in the Introduction. The same creep ruptured specimen was cut along longitudinal direction on (110) plane and mechanically polished using 1-μm diamond powder spray followed by electrochemical polishing using Struers LoctroPol5 operated at 45 V for 6 s with a solution of 10 vol. % perchloric acid in methanol under 45 V at around 4 °C. A Zeiss Crossbeam 540 FEG-SEM with Gemini 2 column was used to obtain an electron channeling contrast image (ECCI) on this creep ruptured CMSX-4 Plus specimen for observation of dislocations inside and outside of the microstructure coarsened band. The images were acquired at an accelerating voltage of 30 kV and probe current 5 nA with a stage tilt of 7°. The same specimen was analyzed by EBSD using JEOL JSM-6100 SEM with EDAX detector controlled by the TSL OIM software.

2.3.Scanning transmission electron microscopy

Thin disc-like plates for microstructural investigation were cut from the middle of the gage section perpendicular to the loading axis of the specimens (plane normal to [001] direction) using a precision cutter with an abrasive disc. The discs having a 3 mm diameter were ground on a P4000 SiC abrasive papers down to a thickness of 70-100 µm. Then, they were electropolished in a twin jet polishing system Struers TenuPol5. The electrolyte containing 5% perchloric acid ($HClO_4$) and 95% of glacial acetic acid (CH_3COOH) (by volume) was used. The optimum polishing conditions were obtained at 70 V, 170-200 mA and temperature of 12 °C.

Scanning transmission electron microscopy (STEM) was used for multi-scale high-resolution characterization of the microstructure at length scales down to nanometers. STEM foils tilted into specific low index crystallographic zones were investigated using an image-aberration corrected and monochromated Thermo Fisher Scientific (TFS) Titan-Themis 30-300 kV S/TEM. Defect contrast was obtained by low-angle annular dark-field (LAADF) STEM or by two-beam diffraction contrast imaging (DCI) using both bright field (BF) and high-angle annular dark-field (HAADF) STEM detectors [38]. By simply adjusting the microscope camera length, and thus the acceptance angle of the annular detector, it was possible to transit from HAADF Z-contrast imaging mode performed by exclusively collecting electrons which have been scattered to high angles to the small-angle scattered electrons sensitive to defect contrast [39]. Specific crystal orientations and excited diffraction vectors forming diffraction contrast in LAADF/BF-STEM DCI were determined from corresponding reciprocal space Kikuchi band patterns and by using the convergent beam electron diffraction (CBED).

Tilting experiments were combined with the stereo STEM-DCI microscopy to evaluate the crystallography and the spatial distribution of defects [40,41]. Stereo method is based on providing separate images for both eyes of the observer. The two images of a stereogram are taken at two angular positions of the foil and the corresponding rotation angle is close to viewing angle of the observer. When exploiting DCI in stereo STEM, two micrographs need to be taken at the same magnification and under the same two-beam diffraction contrast condition. Two stereo STEM-DCI micrographs are color coded using the freeware Anaglyph Maker Version 1.08 to obtain a 3D anaglyph [41,42]. Using a special pair of red-cyan colored glasses yields the correct 3D impression. The data were collected and processed using the TFS Velox software. In particular, the STEM images were corrected for possible drift and scanning beam distortions using the drift corrected frame integration (DCFI) function of Velox.

Chemical composition was analyzed from the data collected by Super-X energy dispersive X-ray spectroscopy (EDS) detector in Titan-Themis STEM. The data were collected and processed using the TFS Velox software. In particular, the raw data in the original spectral maps were quantified using standard Cliff-Lorimer (K-factor) fit (default k-factors available in Velox were used as well as the Brown-Powell empirical ionization cross-section model), including absorption correction and background subtraction.

3. RESULTS

3.1.Pre-deformation of Ni-based SX superalloy specimens

Stress-strain curves associated with the tensile pre-deformation of Ni-based SX superalloys (as-solutioned AM1 and CMSX-4 Plus, and fully heat treated AM1) are plotted in **Fig. 3**. In the as-solutioned state, AM1 has higher yield strength at RT compared to that of CMSX-4 Plus, which is consistent with the tensile properties of the same alloys after full heat-treatment reported in previous studies [43,44]. The 3rd gen. Ni-based SX superalloys generally have a lower APB energy than the 1st gen. superalloys, and therefore, γ' precipitate shearing can occur at lower stress [43–45]. The highest yield stress achieved by AM1 after aging treatments (AM1-HT-RTPD) is a result of optimized size and shape of γ' precipitates during aging HTs [5,43,46,47]. γ/γ' microstructure optimization is generally designed for creep properties; however, this also improves yield strength of <001> oriented Ni-based SX superalloys at RT [5,47].

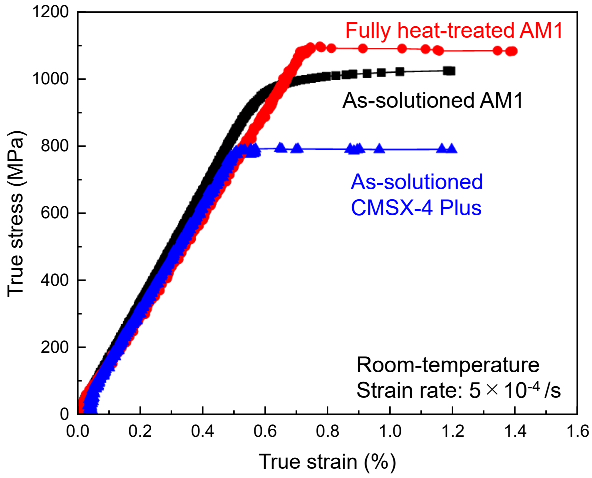

Figure 3. True stress-true strain curves obtained by a tensile PD at RT with a strain rate 5×10^{-4} s^{-1} on AM1 (without and with HTs) and CMSX-4 Plus (without HT).

The surface of the cylindrical specimens after pre-deformation was investigated using optical microscopy and the results are shown in **Figs. 4(a-c)**. Density of observable shear bands has inverse correlation to the yield strength of a material, i.e., increasing yield strength with decreasing density of observable shear bands in the cylindrical surface. The density of shear bands affects microstructure after the first stage aging treatment as shown in **Figs. 4(d-f)**. Diagonal lines observed in these low magnification images are the microstructure coarsened bands where γ/γ′ microstructure evolution has been promoted significantly due to an elastic strain around slip bands. Such contrast is revealed because of different precipitate sizes. Representative micrographs of the microstructure coarsened bands are shown in **Fig. 5**. The thickness of the bands has a range of 2-20 μm for both AM1-PD-A1 and 4P-PD-A1 specimens, and it can be up to 250 μm for AM1-HT-PD-A1 specimen.

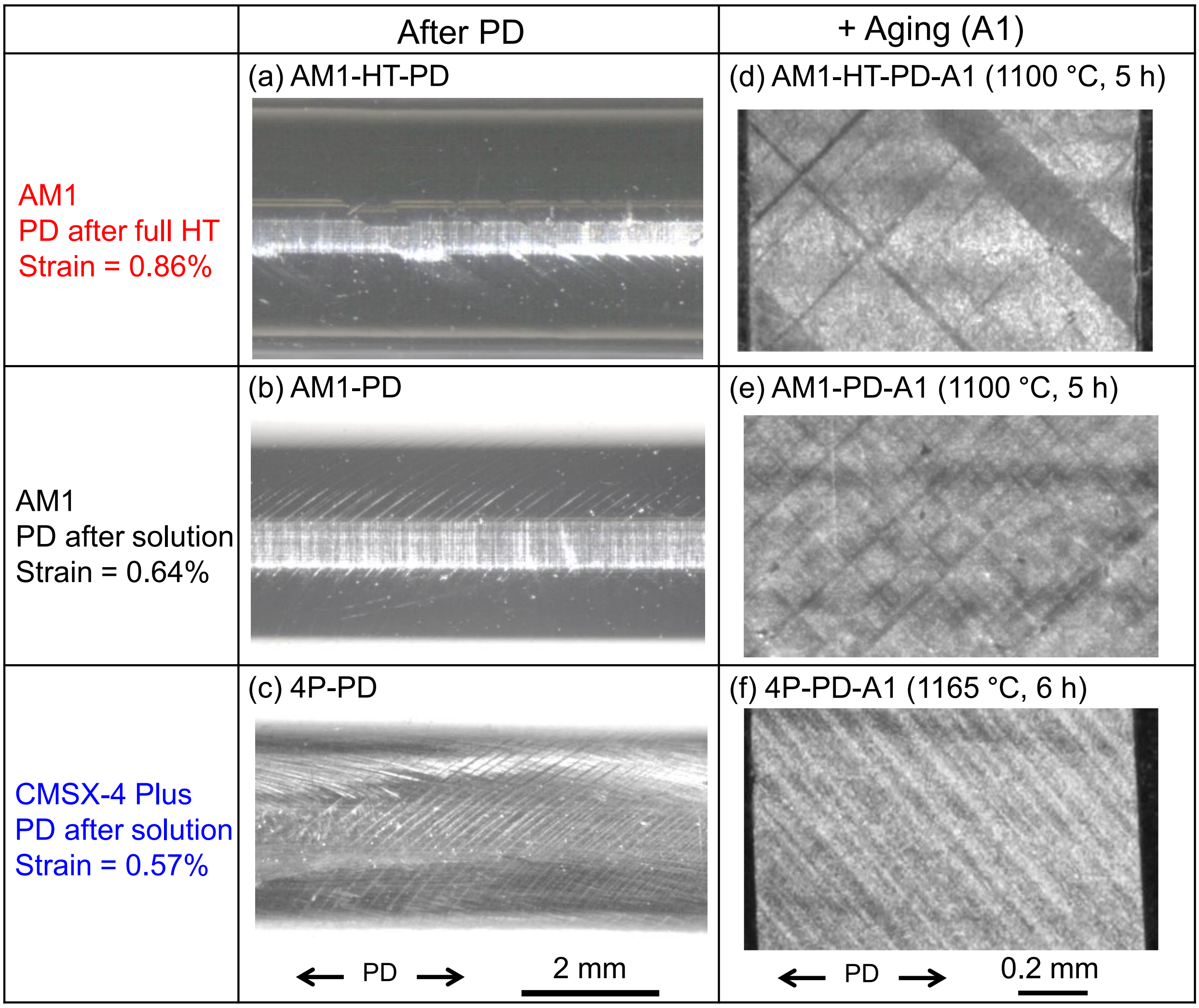

Figure 4. (a-c) Appearances of the cylindrical specimens' surface after pre-deformation as inspected by optical microscope. (d-f) Detail of the microstructure of the same specimens after aging treatment at 1100 °C for 5 h or 1165 °C for 6 h.

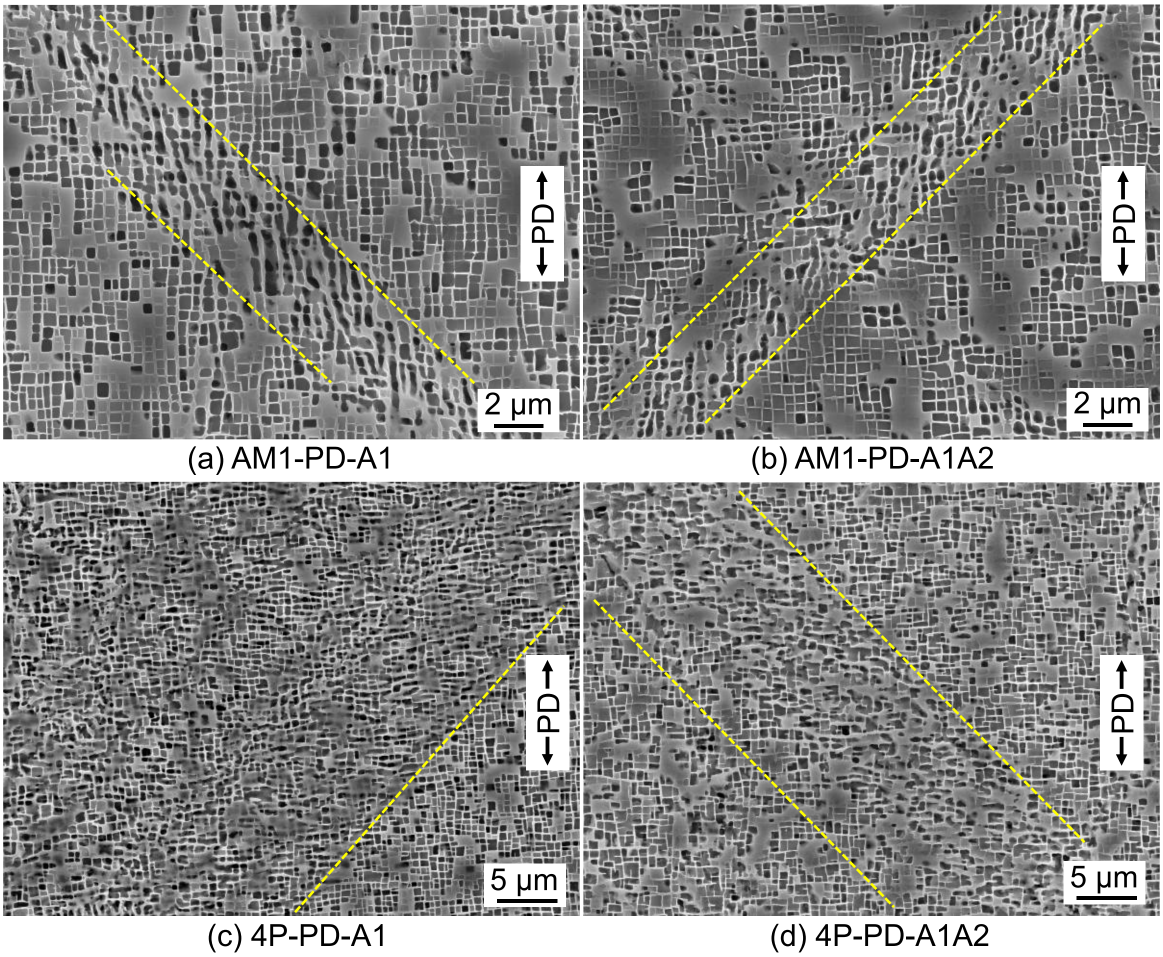

(a) AM1-PD-A1 (b) AM1-PD-A1A2

(c) 4P-PD-A1 (d) 4P-PD-A1A2

Figure 5. Micrographs of pre-deformed AM1 (a, b) and CMSX-4 Plus (c, d) after first (a, c) and second (b, d) aging HTs. Plastic strain for AM1 is 0.79% and that for CSMX-4 Plus is 0.86%.

3.2. γ′ precipitate size and morphologies after the heat treatments

Representative microstructures of pre-strained (~0.8%) AM1 and CMSX-4 Plus after first and second aging HTs are shown at the length scales corresponding to several tens of precipitates in **Figs. 6(a, b)** and 7**(a, b)**, respectively. Yellow dashed lines designate the border between typical cuboidal γ/γ′ microstructure and evolved microstructure which is a consequence of a pre-deformation. Examples in **Figs. 6(a, b)** and 7**(a, b)** are the selected cases where the border is easily identified. However, in some regions where there are only one or two cuboidal γ′ precipitates between the bands, the borders can be unclear. Those examples of difficultly identifiable band are shown in **Fig. 4(f) and Fig. 5(c)**.

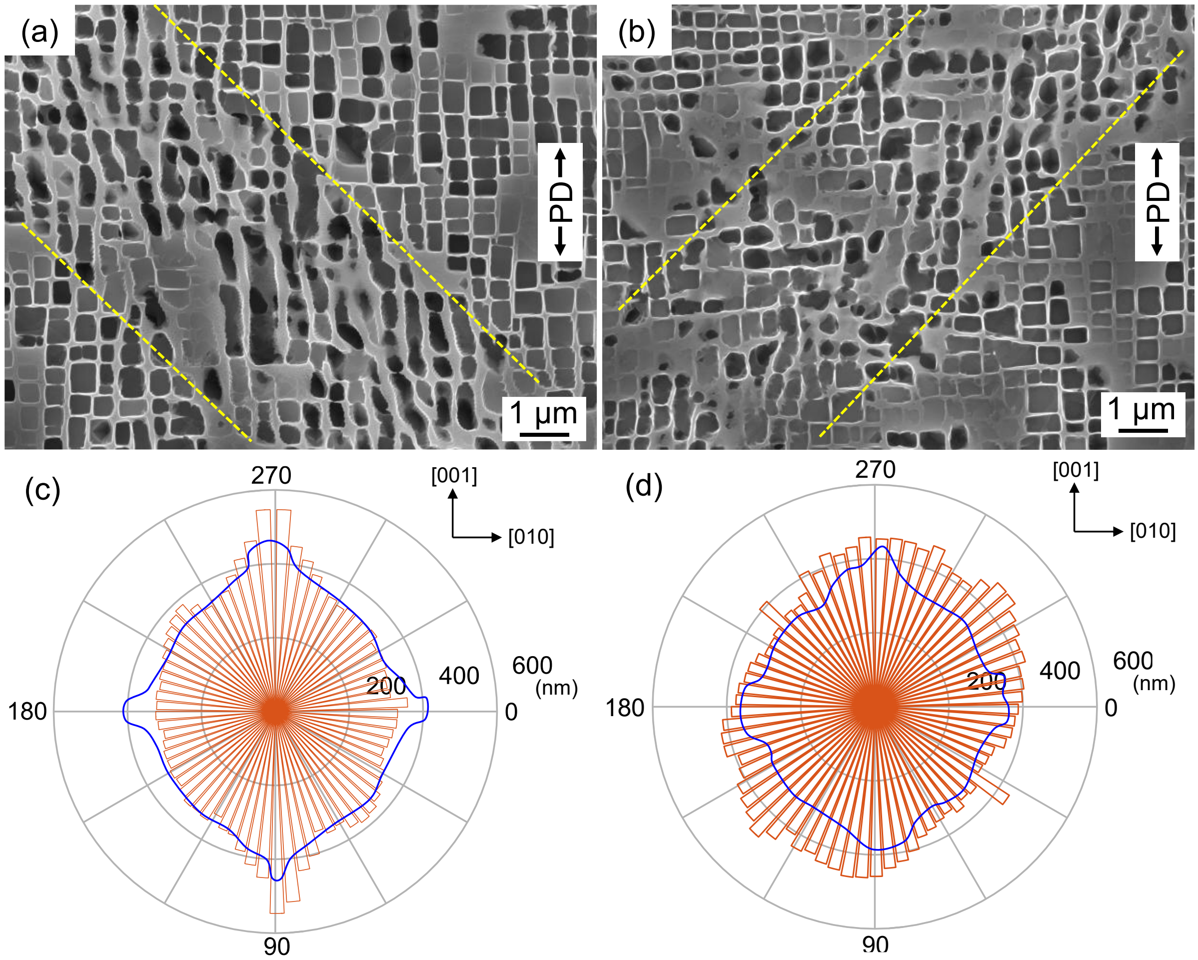

AM1-PD-A1
1100 °C, 4 h

AM1-PD-A1A2
1100 °C, 4h → 870 °C, 16 h

Figure 6. SEM-SEI micrographs of representative microstructure (a, b), and the results of the RIM-X analysis (c, d) of pre-strained (0.79%) AM1 followed by aging HTs. (a) and (c) are after the first stage aging HT. (b) and (d) are after the first and second stage aging HTs. Rose diagrams represent γ′ precipitate sizes inside the microstructure coarsened band and overlayed blue curves show sizes of cubic γ′ precipitates outside the band.

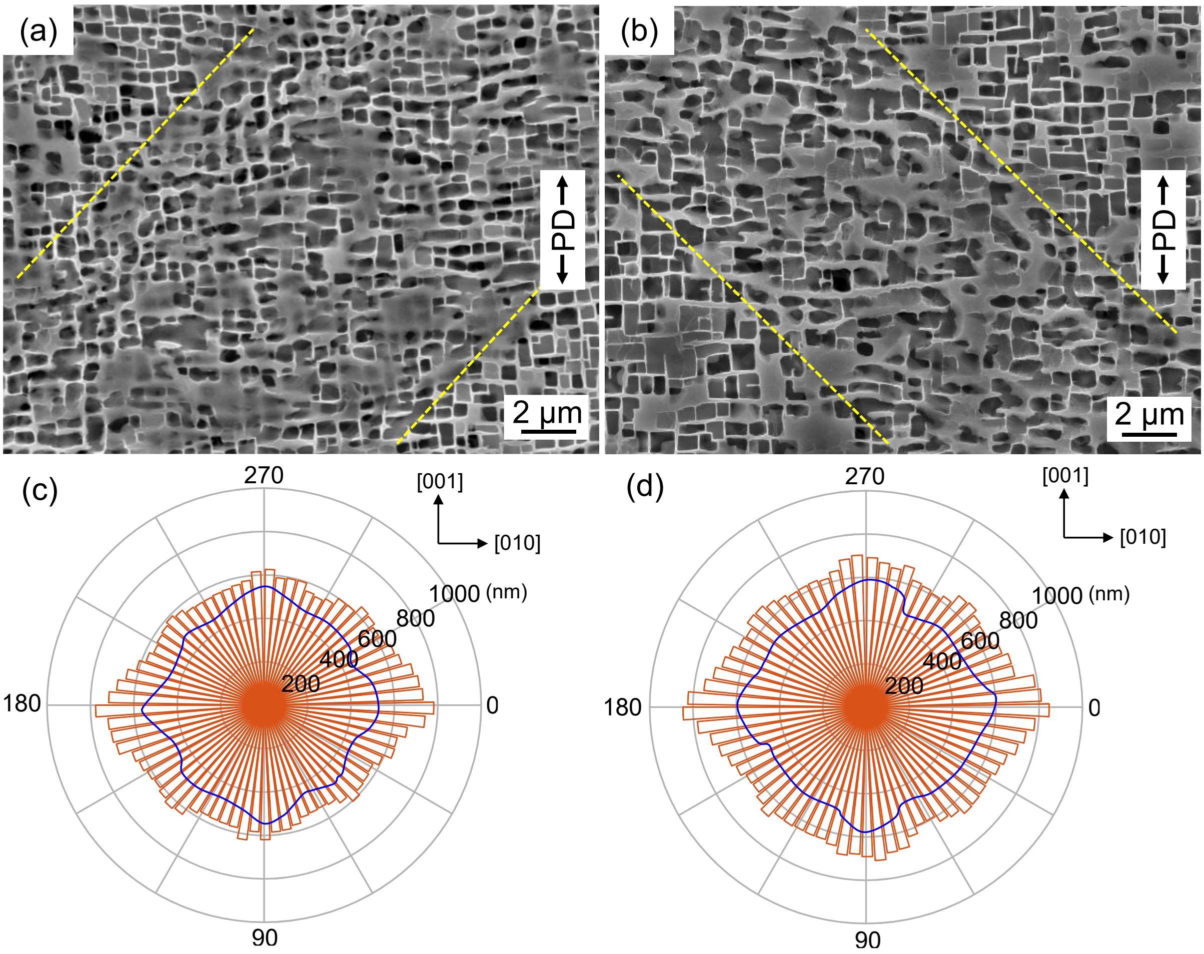

4P-PD-A1
1165 °C, 6 h

4P-PD-A1A2
1165 °C, 6 h → 870 °C, 20 h

Figure 7. SEM-BSE micrographs of representative microstructure (a, b) and the results of RIM-X analysis (c, d) of pre-strained (0.86 %) CMSX-4 Plus followed by aging HTs. (a) and (c) are after the first stage aging HT. (b) and (d) are after the first and second stage aging HTs. Rose diagrams represent γ′ precipitate sizes inside the microstructure coarsened band and overlayed blue curves show sizes of cubic γ′ precipitates outside the band.

The size of γ′ precipitates in different directions was characterized for the microstructures shown in **Figs. 6(a, b) and 7(a, b)** by RIM-X software [36,37]. Precipitate sizes for those inside the microstructure coarsened band were carefully measured by selecting γ′ precipitates that are affected by the pre-deformation, and not relying on the dotted lines shown in Figs. 6 and 7. Results of RIM-X analyses on γ′ precipitates within the microstructure coarsened band are presented as a rose diagram and that of cubic precipitates outside the band is overlayed as a blue curve. Each bar of a rose diagram shows average γ′ size of intercepting line drawn along the determined angle (every 5°). Both rose diagram and overlayed curve also represent shapes of γ′ precipitates. If the precipitate is cuboidal, rose diagram is near square shape 45° rotated with respect to 0° (see blue curves in **Figs. 6(c, d)** and 7**(c, d)**). This means cubic precipitates outside the band have a major edge length in [001] (0°/180°) and [010] (90°/270°) crystallographic directions. When a rose diagram has one preferential direction (0°/180° or 90°/270°), it means the precipitates in the analyzed area have a tendency of either N-type (transverse to the loading direction) or P-type (parallel to the loading direction) directional coarsening [48].

The rose diagram of AM1-PD-A1A2 in **Fig. 6(d)** shows an oval with 45° rotation (135°/315° directions) which is the parallel direction to the microstructure coarsened band. This quantification suggests that γ′ precipitates in the microstructure coarsened band of AM1-PD-A1A2 have elongated in both vertical and horizontal ([001] and [010]) directions equally. In the case of AM1-PD-A1 (**Fig. 6(c)**), the γ′ precipitates showed slight evolution in 45°/225° directions with stronger tendency of a P-type γ′-rafting (0°/180°).

Previous study showed that γ′ precipitate evolution of AM1 mainly occurred during the first stage HT where precipitation growth is more active at higher temperature (1100 °C), associated with dislocation grooves exposed by etching and observed at the γ/γ′ interface (see **Fig. 8**) [25,49,50]. Secondary HT at 870 °C only changed the γ′ volume fraction (from 50% to 57-60% [32]) and had a minor effect on the precipitate sizes. This is also demonstrated in the same measurement using the RIM-X where the γ′ precipitate sizes are similar for both AM1-PD-A1 and AM1-PD-A1A2 regardless of positions, inside or outside the microstructure coarsened band.

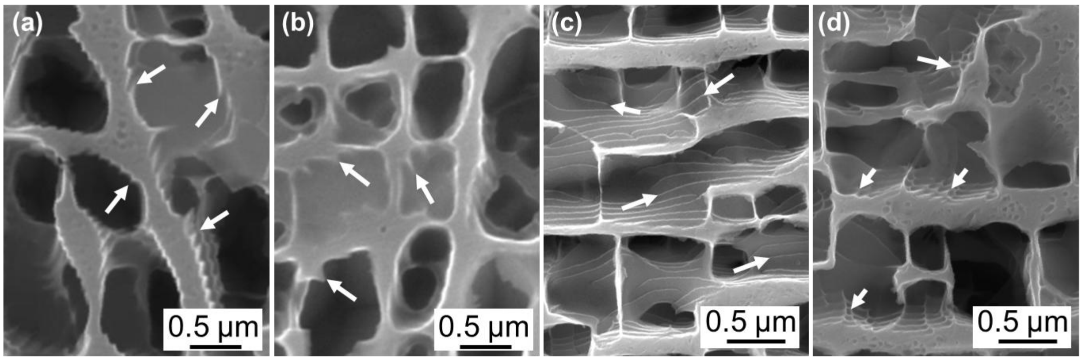

Figure 8. Examples of γ/γ′interfacial dislocation grooves observed in pre-deformed materials after heat treatments. (a) AM1-PD-A1, (b) AM1-PD-A1A2, (c) 4P-PD-A1, (d) 4P-PD-A1A2.

The same RIM-X analysis was performed for pre-deformed CMSX-4 Plus after two different HT stages and the results are shown in **Figs. 7(c, d)**. Because the first stage HT was at a higher temperature 1165 °C and for a longer duration 6 h, cubic γ′ precipitate size of CMSX-4 Plus (500-600 nm) is much larger than that of AM1 (350-450 nm). Although the γ′ precipitates are heavily coarsened after the first stage HT (**Fig. 7(c)**), they tend to maintain rectangular shape in the observed plane (i.e. major edge length in [001] (0°/180°) and [010] (90°/270°) directions), and the small increase of the γ′ size during the secondary HT was just a consequence of increasing γ′ phase volume fraction (from 52% to 65-70% [32]). Aging of pre-deformed CMSX-4 Plus leads only to precipitate coarsening and coalescence of nearby precipitates, and γ′-rafting type coarsening is not pronounced when compared to that in AM1.

3.3.STEM multi-scale characterization of the microstructure

In order to understand the microstructure evolution mechanisms during the development of the microstructure coarsened band, STEM coupled with EDS was employed for characterization of the dislocation microstructures of two experimental alloys with different thermal histories as described in **Table 3**. Characteristic microstructures are presented using the technique of the 3D stereo-pair anaglyphs to help with the identification of the locations of dislocations as observed by STEM-DCI.

The microstructure of AM1 after pre-deformation is shown in **Fig. 9**. Stereo-pair BF-STEM DCI in **Fig. 9(a)** reveals paired dislocations shearing γ′ precipitates in typical $\frac{a}{2}\langle 110\rangle\{111\}$ systems. The thin slip band in **Fig. 9(b)** shows a trail consisting of dislocations within the γ matrix, paired dislocations shearing γ′ precipitates, and isolated dislocations. Thick slip band having a 20-30 μm width along [010] direction in **Fig. 9(c)** revealed interaction of paired dislocations in multiple slip systems and also planar faults.

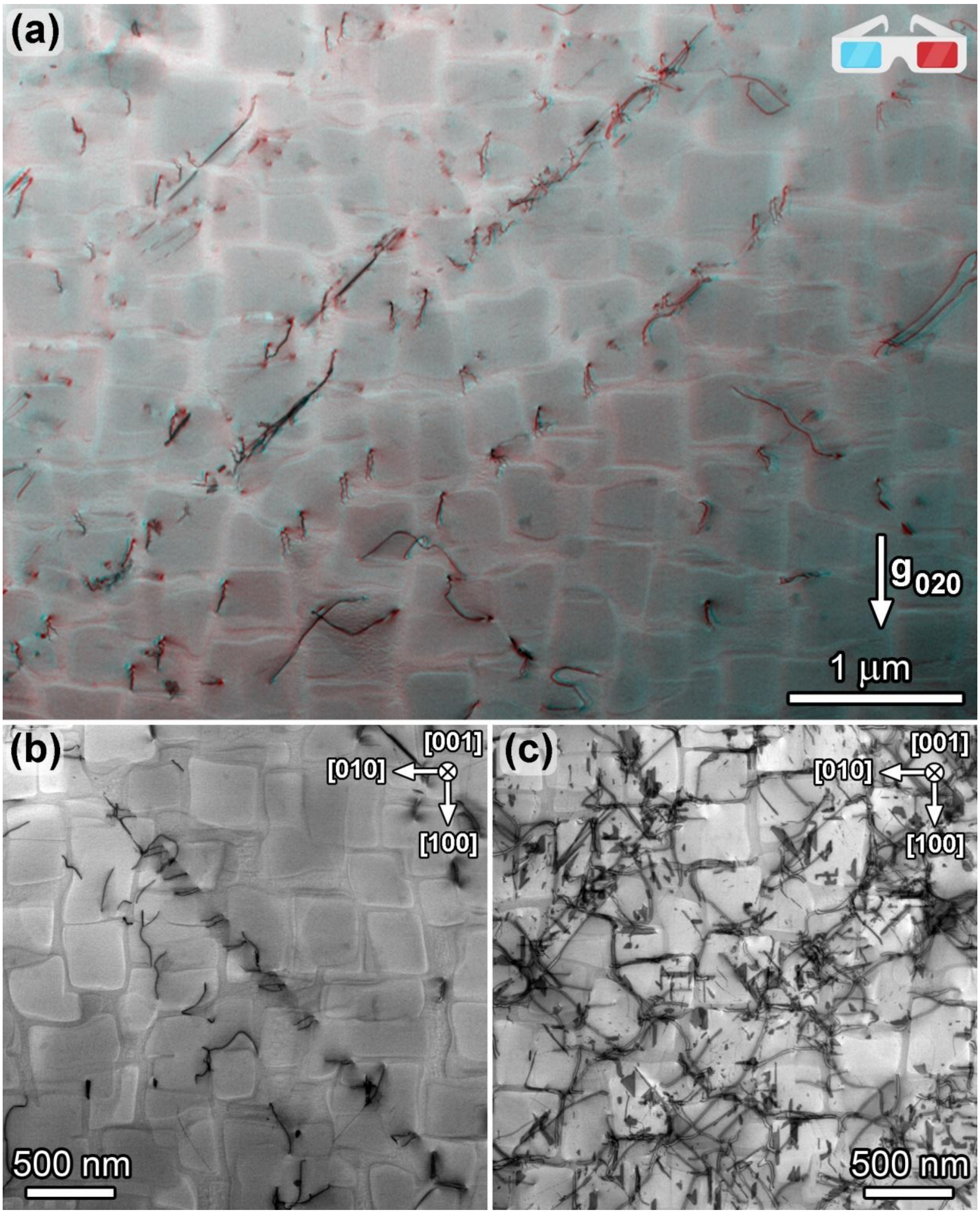

Figure 9. Characteristic microstructure of AM1 after PD with 0.79% plastic strain (no aging heat treatment, AM1-PD). (a) BF-STEM DCI stereo-pair anaglyph showing paired dislocations in thin deformation bands shearing precipitates. (b, c) BF-STEM DCI obtained with electron beam direction parallel with [001] zone axis revealing thin (b) and thick (c) deformation bands containing paired dislocations and planar faults. (Color figure online)

BF-STEM DCI micrograph in **Fig. 10(a)** shows the microstructure coarsened band in the pre-deformed AM1 after the first stage HT (AM1-PD-A1). After the first stage HT, complex dislocation arrangements are observed mainly at the γ/γ′ interfaces. Interfacial dislocations and 60° type matrix dislocations are similar to those reported for very early primary creep stage of Ni-based SX superalloys under high temperature/low stress creep conditions, generally between 1000-1150 °C [51–53]. Two γ channels oriented parallel with [010] crystallographic direction in **Fig. 10(a)** (highlighted by white dashed rectangles) are the ones that the dislocations are spreading from the core of the band toward the direction of the long arrows. Some dislocations are already entering into the γ′ precipitates and connecting γ channels on the other side of a precipitate; examples are pointed by black arrows in **Fig. 10**. Short white arrows are pointing to the interfacial grooves occupied by dislocations that are also reported in a Ni-based SX superalloys with prolonged aging at temperatures above 1100 °C [54,55] or early stage of creep plasticity [49,56].

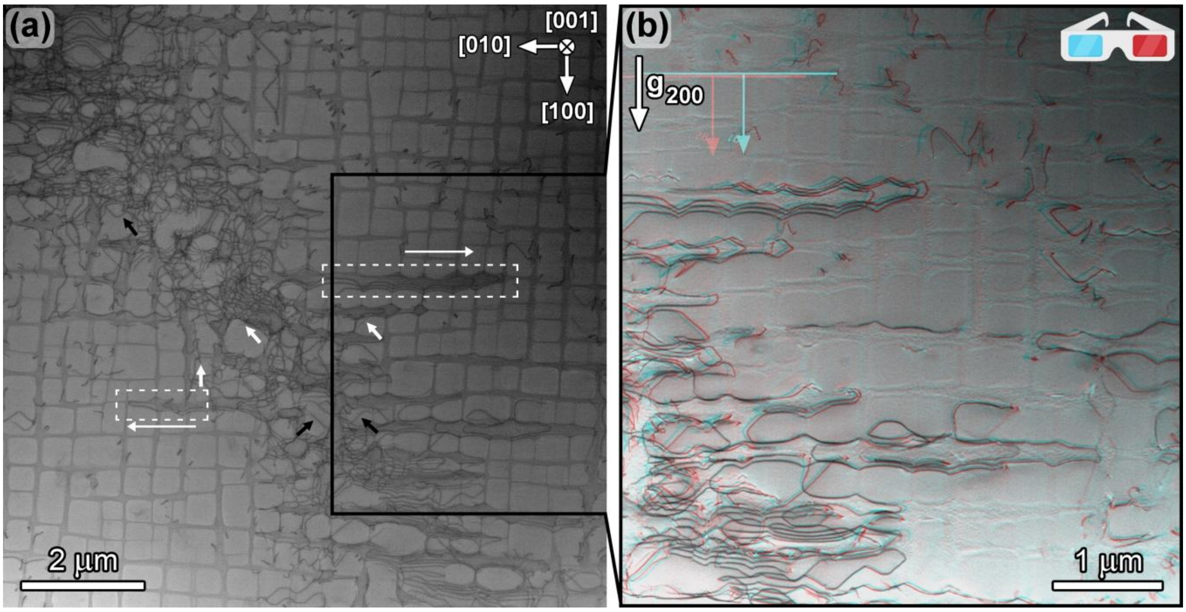

Figure 10.(a) BF-STEM DCI of AM1-PD-A1 (plastic strain 0.86%, at 1100 °C for 5 h) obtained with electron beam direction parallel with [001] zone axis. (b) Corresponding 3D stereo-pair anaglyph. Black arrows are pointing at dislocations inside the γ′ precipitates and white arrows are dislocation grooves at γ/γ′ interface. (Color figure online)

Details of this area are shown as 3D stereo-pair anaglyph in **Fig. 10(b),** and it reveals that the dislocation lines of spreading dislocations (white dotted section in **Fig. 10(a)**) are forming curves that reflect the shape of a γ channel. Matrix channel with the spreading dislocations is thicker and the channels perpendicular to the spreading dislocations are thinner than the other channels around cubic γ′ precipitates. 3D visualization of two dislocation types mentioned above (black and white arrows) proves that they are located inside the γ′ precipitate.

To complement the information from the diffraction contrast imaging of the defect structure, also STEM-EDS compositional line profiles were acquired along two arrows B and C drawn in **Fig. 11(a)** (detail of BF-STEM DCI in **Fig. 10(a)**). Line profile B (**Fig. 11(b)**) is intersecting with spreading dislocations and line profile C is intersecting with dislocation-free γ channels (**Fig. 11(c)**). Dislocation free γ channels in both line profiles B and C are showing similar local chemical compositions with typical Cr and Co (γ-former) segregation [25,57,58]. Middle "macroscopic" peak of Cr and Co in **Fig. 11(b)** corresponds to the broadened γ channel and further reflects its curved shape. The respective positions of dislocation lines of three spreading interfacial dislocations were marked into the EDS line scan by black dashed lines for reference. The same was done for small individual dislocation segments entering γ′ precipitate (see black arrow in both **Figs. 11(a)** and **(c)**). The phenomenon of elemental (Cr, Co, and others) segregation to dislocations has been reported and well established in the literature and its impacts on the directional coarsening are widely accepted in the community[25,57–60]. Detection of such subtle elemental segregation to one individual defect via electron microscopy is very challenging, however under some circumstances it is not impossible even under non-edge-on crystallographic orientation conditions [61,62]. While potential compositional changes associated with three spreading dislocations in line scan B are on the scale within the error margin of quantified EDS, there is indeed distinct Cr peak on the quantified and integrated line scan C associated with a small dislocation segment entering γ′ precipitate (see black arrow in both **Figs. 11(a)** and **(c)**). This may be due to the fact that the small line segment in γ′ precipitate is actually oriented close to the end-on direction with respect to the electron beam (as determined from the stereo-STEM DCI).

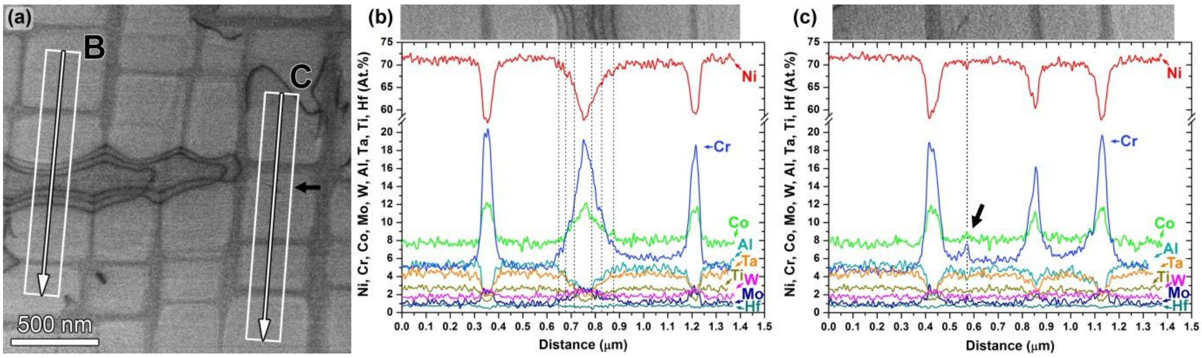

Figure 11.Dislocations extending from the core of the deformation band in AM1 alloy after first aging at 1100 °C for 5 h (A1) (**Fig. 10(a)**). (a) BF-STEM DCI of the inspected area showing positions where two compositional line profiles B (b) and C (c) were extracted using STEM-EDS. (Color figure online)

BF-STEM DCI of the microstructure coarsened band in pre-deformed AM1 after two aging HTs (AM1-PD-A1A2) is shown in **Fig. 12(a)** as a zonal image. **Fig. 12(b)** is two-beam diffraction condition of the same area in **Fig. 12(a)** using g = $[0\bar{2}0]$ in which the majority of the dislocations are out of contrast. The core of the microstructure coarsened band is revealed throughout the image in this two-beam condition since it consists of more complicated dislocation arrangement. Numerous dislocations propagating from the core of the deformation band into the matrix channels are located at the interface of matrix and precipitates. **Fig. 12(c)** is a close-up image of **Fig. 12(a)** and 3D stereo-pair anaglyph of the same area is in **Fig. 12(d)**. From this 3D stereo-pair image, γ/γ′ interfacial dislocations are dense and form networks in the core of the band. Black arrows in **Fig. 12(c)** are pointing at some examples of dislocations that are already inside the γ′ precipitates. STEM-EDS line profile composition analysis across the microstructure coarsened band does not show significant differences between the band and non-affected areas.

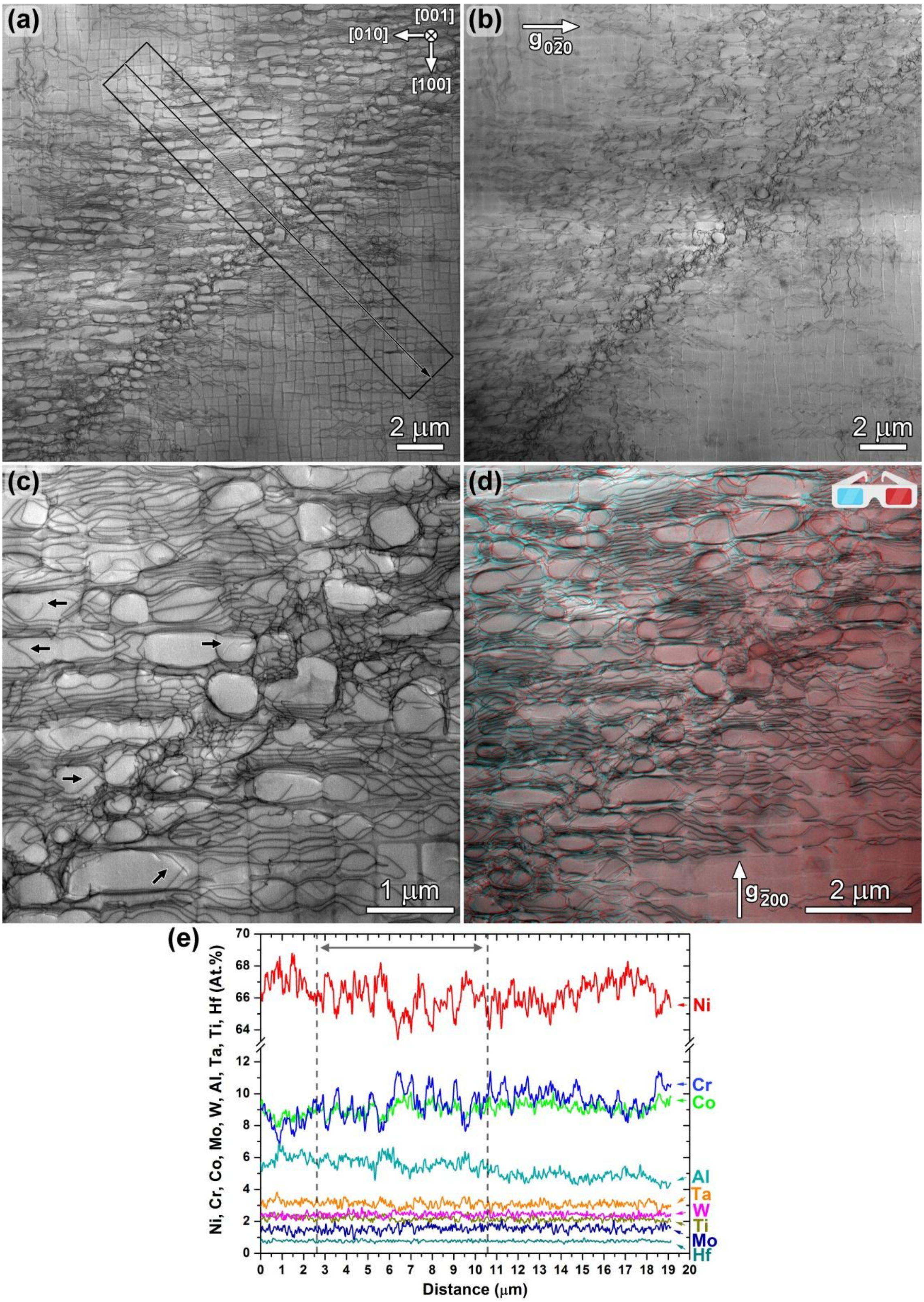

Figure 12.BF-STEM DCI of typical microstructure coarsened band in pre-deformed AM1 after two-stage aging A1 and A2 (AM1-PD-A1A2, plastic strain 0.86%, at 1100 °C for 5 h). (a) Condition with electron beam direction parallel with [001] zone axis. (b) Two-beam diffraction condition using **g** = $[0\bar{2}0]$. (c) Detail of dislocation structure inside

the microstructure coarsened band from (a). (d) Corresponding BF-STEM DCI stereo-pair anaglyph. (e) STEM-EDS line scan along arrow in (a) that is perpendicular to the microstructure coarsened band. (Color figure online)

Similar to STEM observations on AM1, dislocations are observed within γ′ precipitates of the microstructure coarsened band in pre-deformed CMSX-4 Plus after the first stage HT as shown in **Fig. 13**. Development of γ/γ′ interfacial dislocations arrangements and network formation can be observed in **Fig. 13(a)** with some dislocations within γ′ precipitates as pointed by black arrows. **Fig. 13(b)** is another example of the band where the γ′ precipitate is sheared by a superdislocation as visualized by 3D stereo-pair anaglyph.

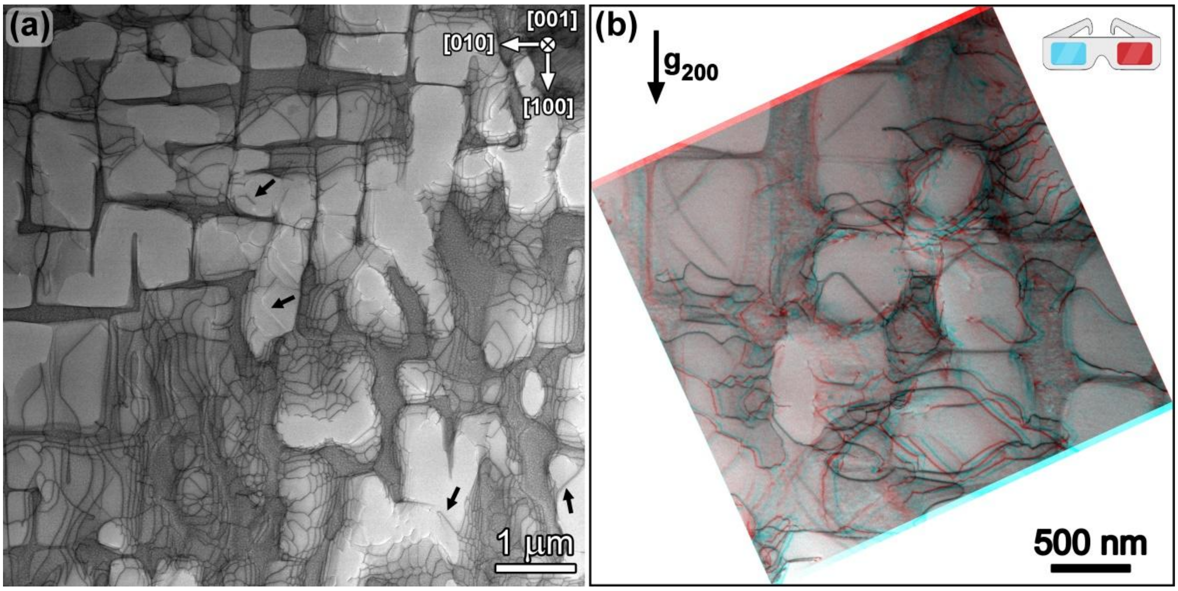

Figure 13.(a) BF-STEM DCI of a microstructure coarsened band in CMSX-4 Plus after PD and first aging HT (4P-PD-A1, plastic strain 0.71%, at 1165 °C for 6 h) obtained with electron beam direction parallel with [001] zone axis. (b) BF-STEM DCI stereo-pair anaglyph showing in detail shearing of a precipitate by superdislocation. (Color figure online)

BF-STEM DCI after RTPD and two stage aging HTs of pre-deformed CMSX-4 Plus is shown in **Fig. 14(a)** and the corresponding 3D stereo-pair image in **Fig. 14(b)**. Black arrows in **Fig. 14(a)** are pointing at some examples of dislocations that are already inside the γ′ precipitates. The analysis of representative microstructure presented in **Fig. 14** demonstrates that γ/γ′ precipitate morphologies and dislocation distribution has not drastically changed during the second aging HT. STEM-EDS compositional line scan in **Fig. 14(c)** shows that average chemistry inside and outside the microstructure coarsened band are similar, in another words, no definitive sign of chemical segregation on the scale of the microstructure coarsened band was found. More distinctive and larger peaks in **Fig. 14(c)** are due to the coarsened irregular precipitates having high density of dislocations. The white dashed rectangle in **Fig. 14(a)** highlights the detail of this morphology as shown in **Fig. 15**.

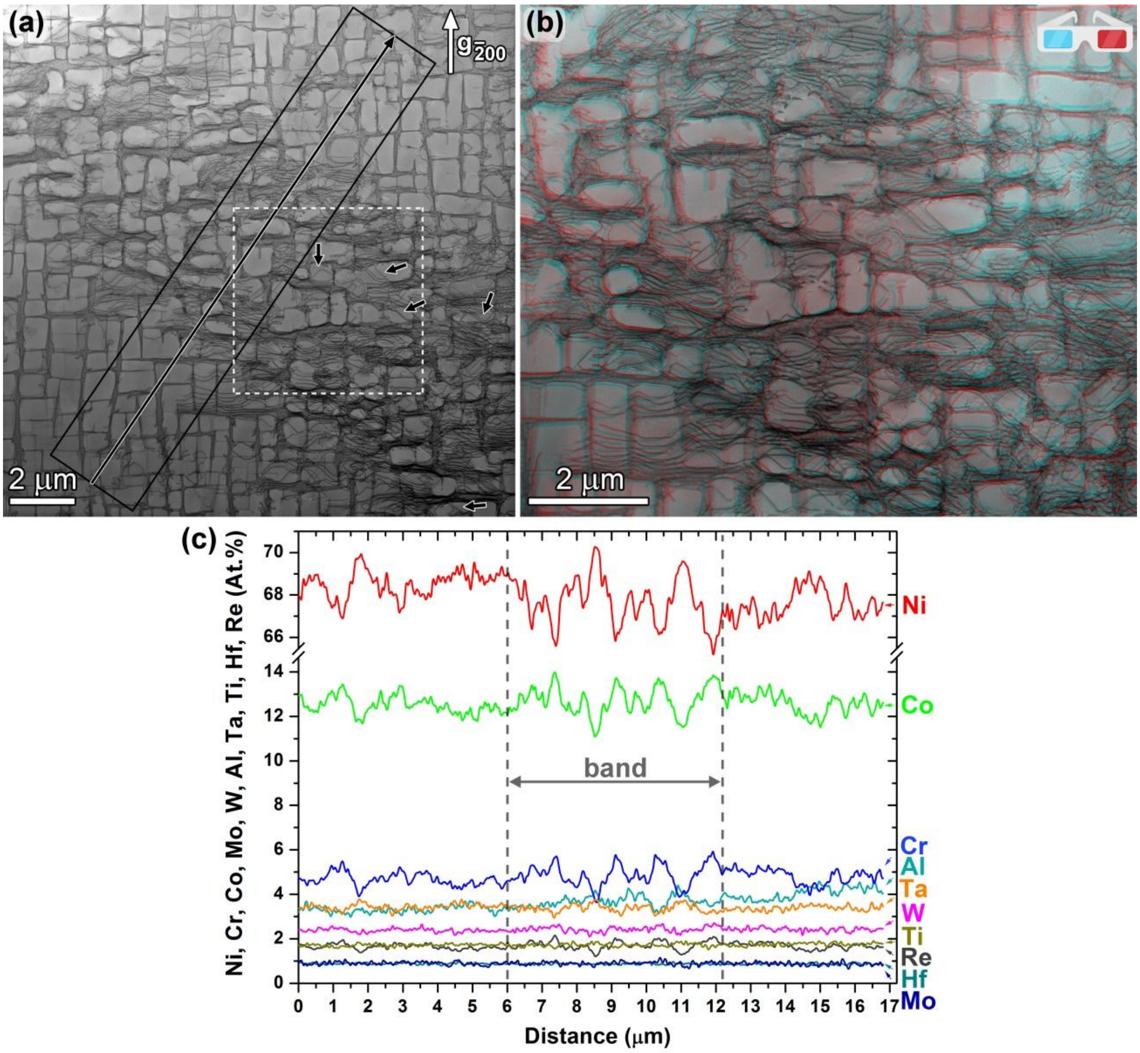

Figure 14.(a) BF-STEM DCI of a microstructure coarsened band in CMSX-4 Plus after PD and two stage aging HTs (4P-PD-A1A2, plastic strain 0.71%, at 1165 °C for 6 h + at 870 °C for 20 h) obtained with electron beam direction parallel to [001] zone axis.

(b) 3D stereo-pair anaglyph showing detail of the same band. (c) STEM-EDS compositional line scan along arrow in (a) that is perpendicular to the microstructure coarsened band. (Color figure online)

Potential compositional changes associated with the areas where γ′-shearing dislocations were identified were investigated in the case of CMSX-4 Plus as well. The compositional line profiles crossing several dislocations within γ′ precipitates (**Fig. 15(a)** and corresponding STEM-EDS map of Cr in **Fig. 15(b)**) were plotted in **Figs. 15(c, d)**. Line profile C is crossing a “horizontal” γ channel parallel with [100] direction that is no longer connected to the “vertical” [010] oriented channel, and it is containing dislocation segments. Multiple paired dislocations which are inside the γ′ precipitate (see stereo-pair anaglyph **Fig. 14(b)**) are analyzed in line profile D. In this specific area with shearing dislocations, the elemental composition inside the γ′ precipitate is altered with notable Cr and Co enrichment at the expense of Ni. Stereo-STEM DCI analysis of the same location demonstrates that the dislocations are shearing γ′ precipitates; however, it is not definitive to say that this area is composed solely of γ′ phase and without presence of γ phase. This can be an extremely thin layer of γ forming elements dragged and bridged by γ′ shearing dislocations.

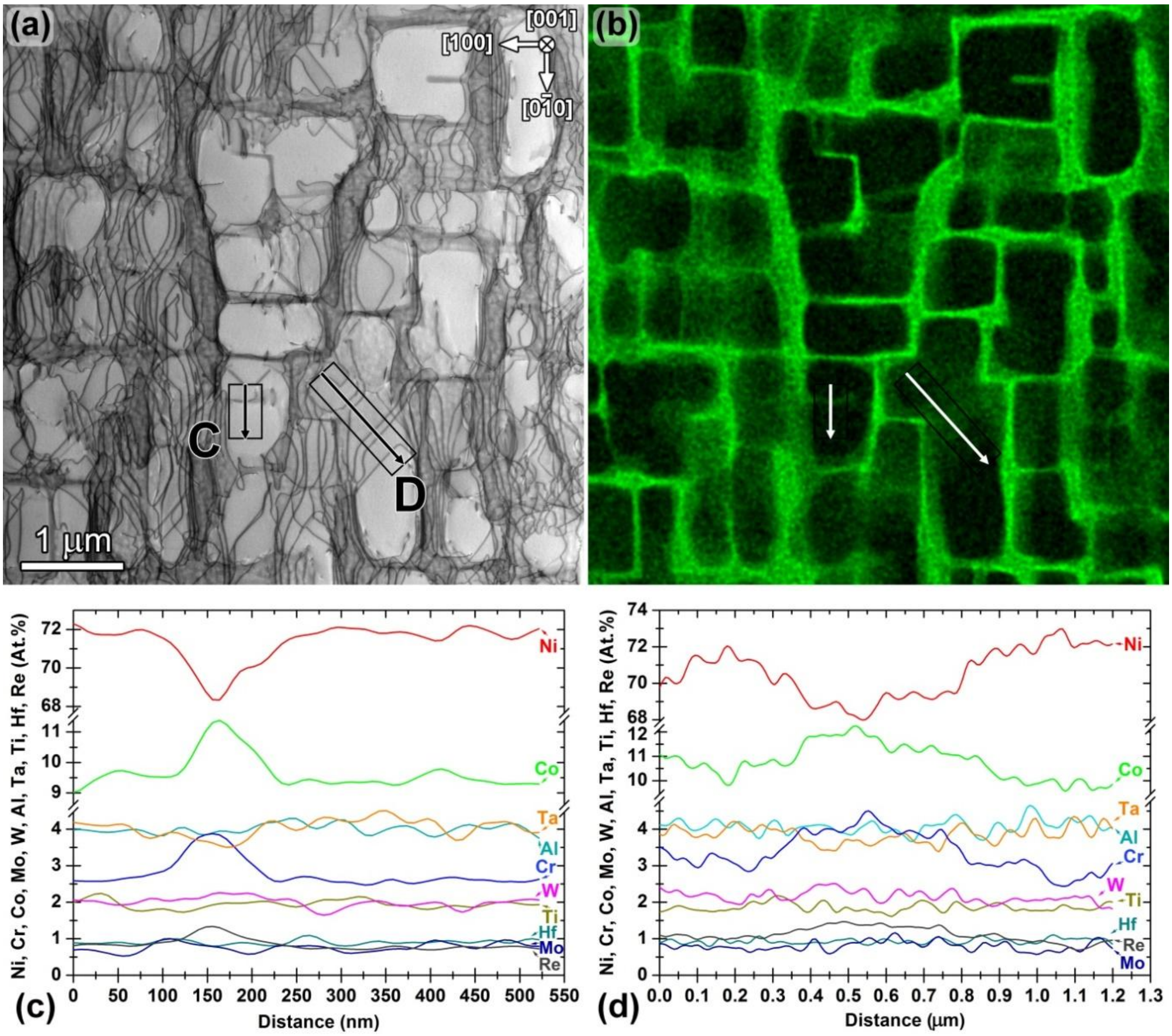

Figure 15. Core of the microstructure coarsened band in pre-deformed CMSX-4 Plus after two-stage aging treatment A1 and A2 (4P-PD-A1A2, plastic strain 0.71%, at 1165 °C for 6 h + at 870 °C for 20 h). (a) BF-STEM DCI of the inspected area shows position where the compositional line profile was extracted using STEM-EDS. (b) Corresponding STEM-EDS map of Cr revealing Cr enrichment in the areas where dislocations are arranged or are shearing the precipitates. (c) STEM-EDS compositional line profile revealing γ-former segregation on unconnected horizontal [100] direction oriented γ channel. (d) STEM-EDS compositional line profile of closely paired dislocations shearing the ordered precipitate. (Color figure online)

3.4.Creep properties analysis on CMSX-4 Plus

Creep curves of pre-deformed CMSX-4 Plus that were reported in the previous study are shown in **Fig. 16** [27]. At 1150 °C (γ′ rafting regime temperature), pre-deformed CMSX-4 Plus showed creep life reduction similar to AM1 crept at 1050 °C. On the other hand, at 1050 °C, creep life of CMSX-4 Plus was not severely affected by the pre-deformation.

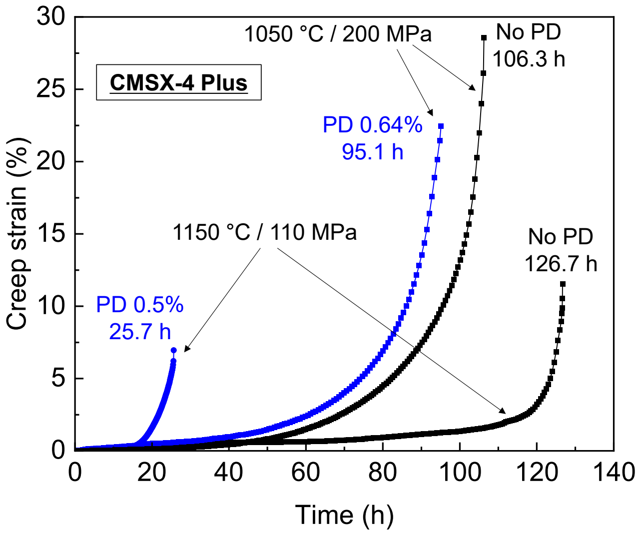

Figure 16. Creep rupture test results of 4P-PD-A1A2 performed at 1050 °C / 200 MPa and 1150 °C / 110 MPa [27].

The results of EBSD analysis performed on crept samples of CMSX-4 Plus are shown in **Fig. 17** to explain the difference between two temperatures 1050 °C and 1150 °C. **Fig. 17(a)** is showing an example of local recrystallization initiated from the creep pores at the microstructure coarsened band. This microstructural feature is identical to the one observed after creep of pre-deformed AM1 at 1050 °C / 140 MPa in the previous study [26], which confirms that the local recrystallization is responsible for the creep life reduction in the pre-deformed CMSX-4 Plus at 1150 °C. When the pre-deformation is not significantly affecting the creep life (1050 °C / 200 MPa), magnitude of lattice rotation is minor, and it is not triggering recrystallisation in the region near the fracture surface (**Fig. 17(b)**). In this case, although some localization is present at the microstructure coarsened bands, the crack propagation is being induced by typical creep voids regardless of their location

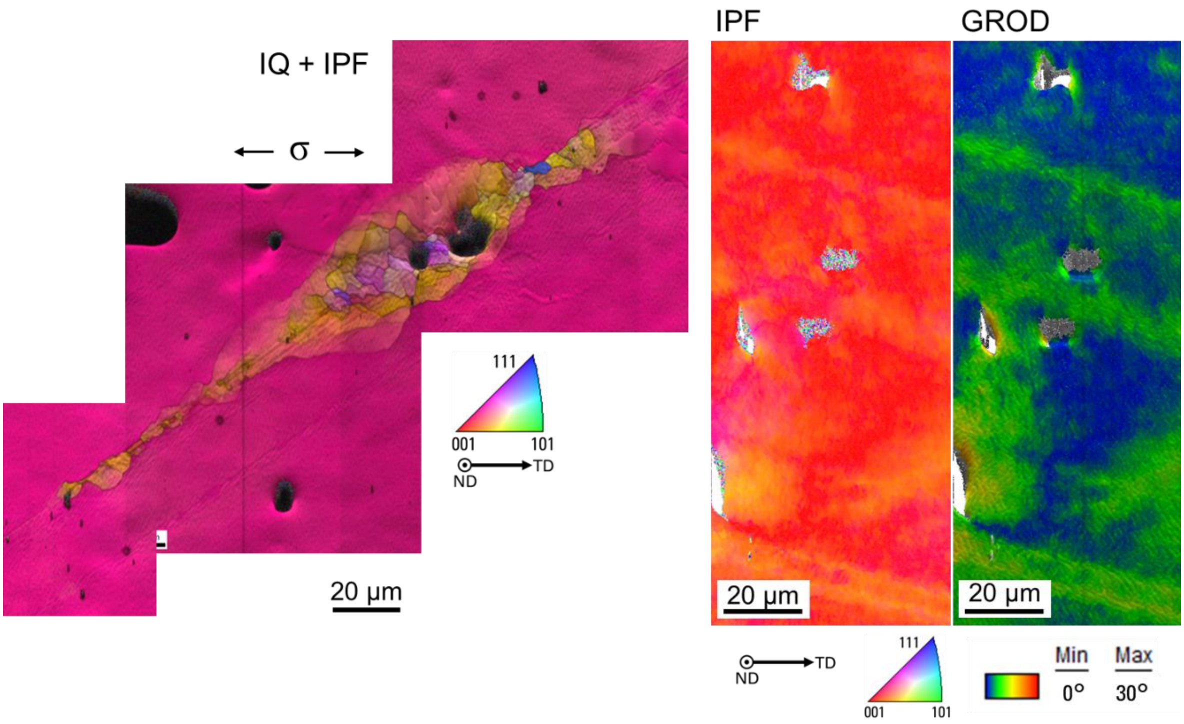

(a) 1150 °C / 110 MPa

(b) 1050 °C / 200 MPa

Figure 17. (a) Inverse pole figure (IPF) color-coded orientation map referring to the tensile direction superimposed on image quality (IQ) map of 4P-PD-A1A2 (0.5% prior plastic strain) after creep rupture test at 1150 °C / 110 MPa. (b) IPF color-coded orientation maps referring to the tensile direction and grain reference orientation deviation (GROD) map of 4P-PD-A1A2 (0.64% prior plastic strain) after creep rupture test at 1050 °C / 200 MPa. (Color figure online)

In addition to EBSD characterization, ECCI was performed on creep ruptured CMSX-4 Plus as shown in **Fig. 18**. Significantly different density of γ′-shearing dislocations were observed inside the microstructure coarsened band (**Fig. 18(a, b)**) compared to the area outside the band (**Fig. 18(b,c)**). γ′-shearing dislocations are mainly on the octahedral system as pointed by white arrows. Additionally, also <001> type dislocation was observed as highlighted by black arrow. These clearly show that creep damage accumulation is faster in the microstructure coarsened band, and it is mainly by dislocation glide on {111} planes. Previous study hypothesized that the creep void nucleation and growth in the pre-deformed AM1 is accelerated by the pipe diffusion at the dislocations in the microstructure coarsened bands [10]. This ECCI observation strongly supports that the dislocations in {111} gliding planes are particularly enhancing the damaging process during the creep deformation under high-temperature low-stress creep conditions.

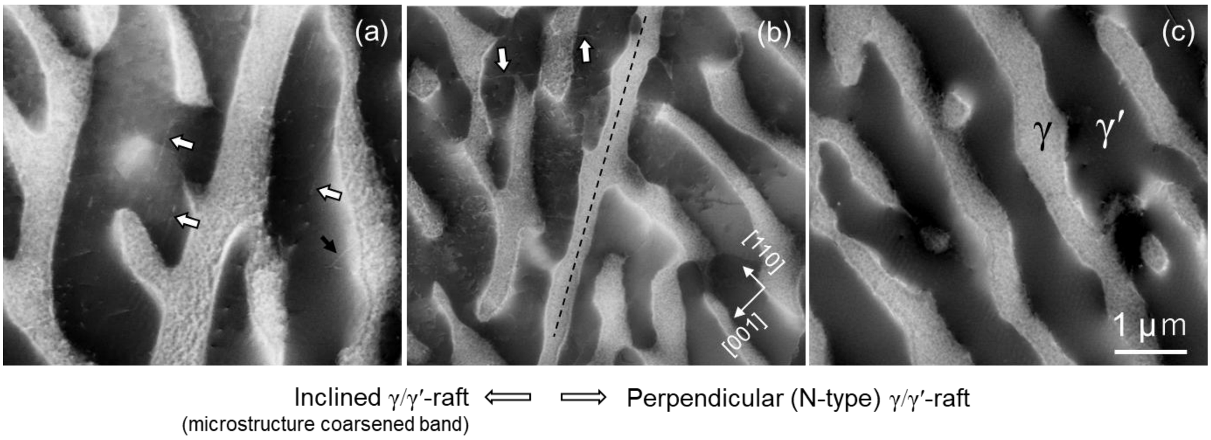

Figure 18. ECCI analysis of the microstructure of CMSX-4 Plus (4P-PD-A1A2, 0.5% prior plastic strain) after creep rupture test at 1150 °C / 110 MPa (loading direction [001]). (a) Inside the microstructure coarsened band showing γ′-raft inclined to loading direction, (b) the border (dotted line along (111) plane) of the microstructure coarsened band and N-type γ′-raft perpendicular to the loading direction, (c) perpendicular N-type γ′-raft outside the microstructure coarsened band. Black and white arrows are pointing at γ′-shearing dislocations. Brighter phase is γ and darker phase is γ′ as indicated in (c).

4. DISCUSSION

Results of detailed multi-scale electron microscopy-based characterization presented in previous sections provide a strong base for the discussion of the processes involved in the microstructure evolution of two different alloys AM1 and CMSX-4 Plus. Three different perspectives are discussed: 1) Tensile pre-deformation behaviors, 2) kinetics of microstructure evolution, and 3) dislocation arrangements and elemental segregations. Having discussed the nature of the microstructure coarsened bands, the origins of creep damage localization [26] at high temperature creep conditions of two SX superalloys are explained.

4.1.Effect of alloy composition on the tensile pre-deformation behaviors

To discuss different pre-deformation behaviors of two superalloys (1st gen. AM1 and 3rd gen. CMSX-4 Plus) in the as-solution treated state, it must be started from tensile yielding behaviors of these alloys. As-solutioned AM1 presents a higher yield strength compared to as-solutioned CMSX-4 Plus. The higher yield strength of AM1 suggests that the resistance to the γ′ precipitate shearing is higher, in another words, more energy is required for the activation of a slip system and to form a slip band during the pre-deformation. Moreover, by full aging treatment that optimizes precipitate morphology, the same alloy AM1-HT1-RTPD presents much higher yield strength. Because slip bands are strongly marked on a surface of AM1-HT1-RTPD (**Fig. 4(a)**) compared to others (**Fig. 4(b, c)**), the local displacement at each single slip band is expected to be larger. When the materials are deformed at RT (i.e. within the γ′-shearing regime) up to equivalent macro plastic strain, material with lower yield strength has a greater number of introduced slip bands, but displacement at each band is necessarily smaller. More and thinner microstructure coarsened bands were observed in former {111} slip planes of CMSX-4 Plus when compared to that in both as-solutioned and heat treated AM1 (**Figs. 4(d-f)**). The thickness and number of the microstructure coarsened bands are evidence that there is a clear distinction in the number of pre-deformation slip bands for these three materials. The above relationship of yield stress, slip band density, and plastic strain magnitude for AM1 and CMSX-4 Plus is schematically presented in **Fig. 19**. On a microscopic scale, elastic strain energy is stored in the stress fields generated by dislocations that interact repulsively and constitute a slip band. With the simplyfing assumption that each slip band contains the same amount of the elastic energy, the color-filled area in **Fig. 19** denotes the stored energy associated with one slip band.

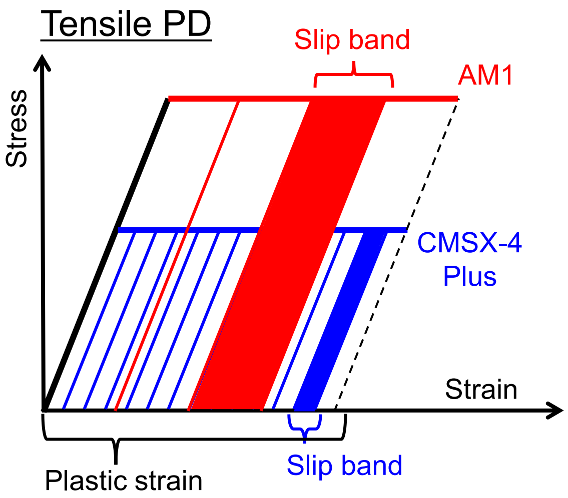

Figure 19.Schematic illustration explaining the relationship between yield stress, slip band density and energy stored in single slip band when comparing as-solutioned AM1 and CMSX-4 Plus alloys.

4.2.Microstructure evolution process of pre-deformed Ni-based SX superalloy

The number of slip bands and stored energy within one deformation band are reflected to the γ′ precipitate shapes/sizes presented in **Figs. 6** and **7**. In these figures, the main points are that: 1) Microstructure evolution mainly occurs during the first stage aging. 2) AM1 showed a stronger tendency of directional coarsening than CMSX-4 Plus.

Two distinctive types of shear bands were observed after pre-deformation; one is collection of thinner slip bands (**Fig. 9(b)**), and another one is a thick deformation band (10-20 μm) with multiple slip planes activated (**Fig. 9(c)**). After the HT of pre-deformed AM1, γ′ precipitate sizes within microstructure coarsened bands are mostly the same regardless of the width of the microstructure coarsened bands. Therefore, during the HT, the type of native dislocation system does not change the precipitation evolution mechanisms. Internal stress relaxation around shearing dislocations and planar faults is a driving force for precipitate evolution that mostly completed during the first stage aging. The area of deformation band (covered by dislocations and planar faults) is a factor determining the width of the microstructure coarsened band.

The microstructure evolution during the first stage aging treatment was very similar to dislocation network development during high-temperature low-stress creep of Ni-based SX superalloys [51,63–65]. The process of γ/γ′ dislocation network formation is known to start by $\frac{a}{2}\langle 110\rangle$ type dislocation climb within γ matrix channels during the primary creep stage [53,66–68]. γ-forming solute elemental segregation (Cr and Co in **Fig. 11**) at the spreading dislocations [57,58] is also suggesting that the process involves diffusion similar to γ′-rafting in AM1. The characteristic of pre-deformed material is that precipitates were penetrated by paired dislocations and planar faults in slip planes (**Fig. 9**) prior to the HTs, and they are not distributed homogeneously over the material volume because the magnitude of plastic strain was only a minor.

Because precipitate plasticity is driven by the similar mechanism as directional coarsening, γ/γ′ lattice misfit at the temperature of first aging treatment needs to be considered to discuss the types of microstructure evolution observed in the band of the two alloys. In general, Ni-based SX superalloy with higher magnitude of lattice misfit will form more planar γ′-rafts during primary stage of high-temperature low-stress creep conditions [53,63]. While AM1 has measured misfit value of about -0.29% at 1100 °C [69,70], that of CMSX-4 Plus at 1150 °C is estimated as -0.2% to -0.25% derived from internal database [71,72]. This estimation is reasonable considering that composition of CMSX-4 Plus is similar to that of CMSX-4 (misfit of -0.2% at 1100 °C) but less Cr and more Re [73,74]. These misfit values suggest that tendency of γ′-raft development can be stronger for AM1, which align with the observations of promoted γ′-rafting in AM1 where one edge length become smaller or similar to cuboid γ′ precipitates (see **Fig. 6(a)**). γ′ coarsening for CMSX-4 Plus has limited anisotropy, but overall, they are consequence of coarsening and coalescence that were accelerated by pre-deformation shear bands.

The fact that γ′-rafting in AM1 was promoted during HT is also indicating the higher stored energy in a slip band for AM1 than that for CMSX-4 Plus. Our previous study that showed 0.3% and 0.8% pre-strained specimen have similar precipitate size evolution during the HTs [25]. This means that the energy involved in microstructure evolution at a single pre-deformation slip band is constant for the same material at such small macro plastic strain, and that further plastic deformation within the single slip tensile deformation regime is just ensured by slip bands multiplication, which justifies **Fig. 19.**

Although the microstructure and dislocation structure evolution processes resemble to directional coarsening at the rafting regime, and it occurred only within 4 to 6 h at high temperature, distinctive characteristics are observed for pre-deformed materials. First feature is the shearing dislocations inside the γ′ precipitates (**Figs 13** and **14**), and second is the creep type void formation reported in the previous study for AM1 [26] (note that creep voids were also observed in 4P-PD-A1A2 before the creep loading). These two features are in fact typically observed at the end of steady state creep regime where diffusion induced creep damages have been accumulated and creep strain starts to increase toward failure [28,29,51,75–84]. However, more importantly, without the applied external stresses like during the creep tests and without full formation of dislocation network, shearing dislocations and creep type voids were already existing in the material. This means that the creep life threatening defects are already forming prior to the creep tests.

4.3. Origin of inclined γ′-rafting and damage localization during high temperature creep

Coarsened microstructure and dislocations configuration are indeed the most important microstructural characteristics that are inherited from as-heat treated pre-strained SX superalloys at the beginning of creep tests. The previous studies have shown that the early creep failure processes of the pre-deformed material are associated with the creep damage localization at the microstructure coarsened band [25,26]. This includes faster microstructure coarsening at the band, earlier and frequent creep void nucleation and growth, and recrystallization around developed creep voids [26]. The same mechanism was observed for CMSX-4 Plus in this study. The following section focuses on the process leading to such localized creep damaging mechanisms, particularly on faster microstructure coarsening at the band, and further details of the creep life reduction occurred in two different alloys AM1 and CMSX-4 Plus.

It is evident that γ′-rafts are inclined along the former microstructure coarsened bands of CMSX-4 Plus at 1150 °C (**Fig. 16**) and AM1 at 1050 °C (**Fig. 1** and references [25,26]). From the observations in this study, it is suggested that inclined γ′-rafts were formed because of dislocation structures induced by the pre-deformation and subsequent HTs. Microstructure after additional prolonged aging of pre-deformed AM1 in **Fig. 20** is heavily coarsened, but long and continuous γ phase can be observed. This is in the same plane as the slip band during pre-deformation. Therefore, inclined microstructure can be naturally formed in the pre-deformed material without presence of the external (creep) load [52,64,85].

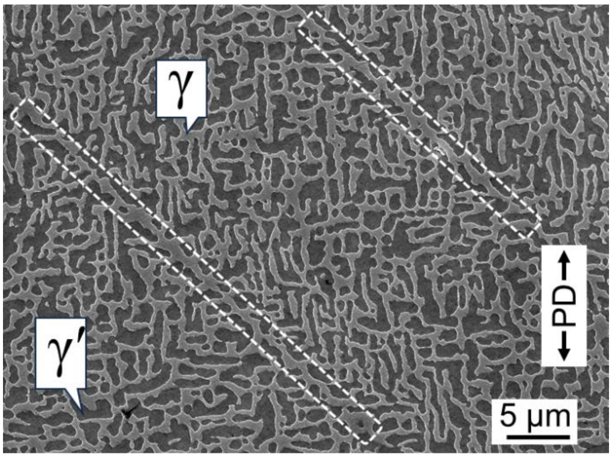

Figure 20. Microstructure of AM1-PD-A1A2 (0.79% plastic strain) after additional prolonged aging at 1050 °C for 500 h. Brighter phase is γ and darker phase is γ′ as indicated in the figure. Areas surrounded by white dotted lines are long and continuous γ-phase.

The process of the inclined γ′-raft formation is indeed associated with dislocation structures observed in this study. Stereo-projection of dislocation structures after heat treatments in **Figs. 10, 12-14** provided evidence of dislocations that are entering into γ′ precipitates from interfacial dislocation network. From STEM-EDS results, these “ready-to-shear” dislocations have typical γ-former segregation. Small interfacial dislocation grooves after the first stage aging are also enriched by γ-formers such as Cr and Co. γ′-raft evolution is known to be promoted by the transportation of these elements through the pipe diffusion process [57,58]. Core of the microstructure coarsened bands (**Fig. 12**) is composed of the complex dislocation structure and hence it has natural tendency of growing toward the former slip plane.

The situation can be more severe during the γ′-rafting regime creep. It is obvious that an external creep load induces inclined rafts that coarsens at a much higher rate, and this can be explained by similar reason to the natural microstructure evolution on {111} planes. The rate controlling elementary process for creep acceleration at the rafting regime is γ′ cutting [28,67,86,87]. The process consists of transfer of γ dislocation segments from dislocation network through the γ/γ′ interface, which then cut through the γ′ phase as a superdislocation. This is followed by dissociation into superpartials that annihilate with the γ dislocation network on the opposing side [67,75,76]. Such dislocation activities are known to make the perpendicular rafts into wavy form at the end of secondary steady stage [58,88,89]. Because “ready-to-shear” γ′-dislocations are already overcoming interfacial barrier, they can easily penetrate through the γ′ phase on {111} plane at an earlier stage of creep deformation [90,91]. Penetrating dislocations can become solute transportation paths to further accelerate coarsening of inclined rafts that acting like wavy rafts at the accelerating stage [58,92]. The higher dislocation density within the band (ECCI observations in SEM in **Fig. 18**) is the direct evidence that this process is locally very active.

Critical effect of “ready-to-shear” dislocations on creep life also aligns with the very high cycle fatigue conditions R = -0.5. The same pre-deformed AM1 showed substantially shorter fatigue lifetime compared to the reference material due to very intense microstructure shearing at the microstructure coarsened bands [93]. The microstructure coarsened band has mobile γ′-dislocations and cyclic fatigue loading (above 500 MPa at 1000 °C) can easily promote further penetration that led to the surface crack initiation.

Another example of microstructure that led to continuous γ phase is shown in **Fig. 21(a)**, which is pre-deformed and creep ruptured CMSX-4 Plus. This area near a developed creep pore has intense shearing traces along the microstructure coarsened band. Because of a large creep pore, stress concentration is expected in this area. If the γ-former solute can transport along an array of shearing dislocation that is the traces, continuous γ phase can form consequently.

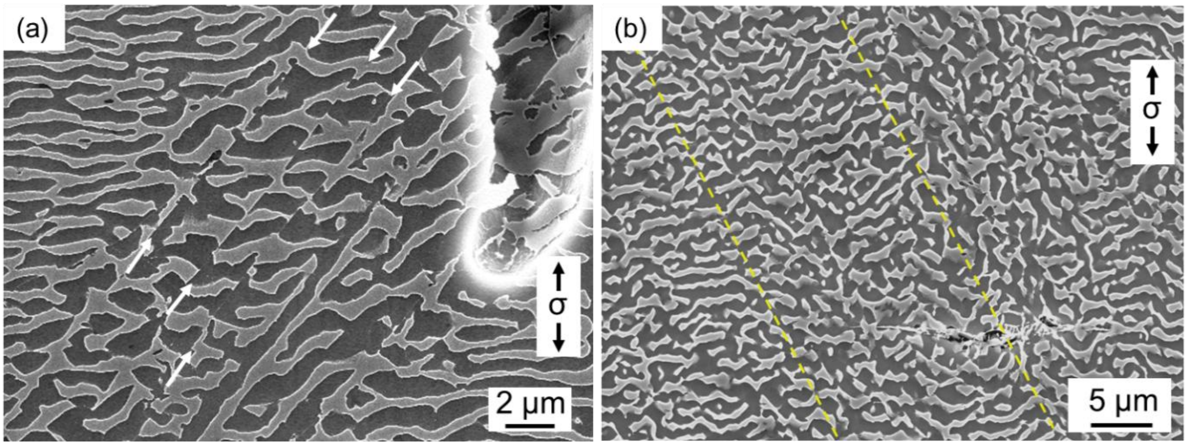

Figure 21. (a) Microstructure of C4-PD-A1A2 (0.5% prior plastic strain) after creep rupture test at 1150 °C / 110 MPa, observed at 2 mm away from fracture plane. Microstructure shearing events are indicated by white arrows. (b) Microstructure of C4-PD-A1A2 (0.64% plastic strain) after creep rupture test at 1050 °C / 200 MPa,

The damage evolving process in the inclined γ′-raft discussed in this section can be schematically illustrated in **Fig. 22**. A creep interrupted test after the primary stage on pre-deformed AM1 [26] showed perpendicular N-type raft and inclined raft at the former slip plane. However, at this point, inclination is not exactly on a {111} plane, and thickness of γ/γ′ layers is not significantly different. Process in **Fig. 22b-1** is explaining dislocation shearing into γ′ phase (**Fig. 18**) that is facilitated by native dislocations developed by RT pre-deformation and subsequent standard aging treatments. Native dislocations have γ-forming solute segregation (**Fig. 15**) and this is also expected for shearing dislocations that help formation of {111} inclined connected γ′-raft structure by solute transportation (**Fig. 22b-2**) [57,58]. The same mechanism accelerates vacancy transportation that leads to rapid coarsening of creep voids [29,81,94,95].

The coarsened and inclined γ′-raft can synergistically enhance the damage process when higher stresses are applied, for example the local stress concentration (**Fig. 21(a)**) or higher creep/fatigue stress cases (AM1 at 850 °C / 500 MPa [25,27] and fatigue stress >500 MPa [93]). In such situations, intense shearing can create a long-connected path for coarsening of the inclined γ′-raft as illustrated in **Fig. 22(c)**.

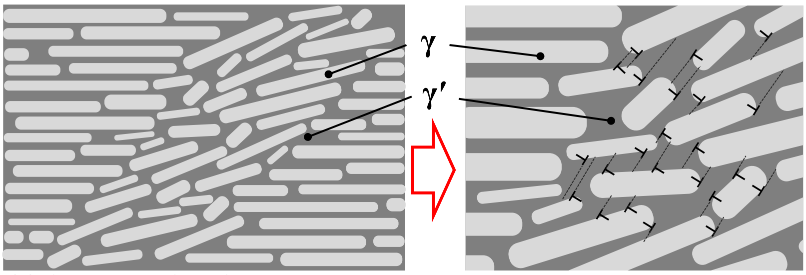

(a) Completion of γ′-rafting and small inclination of γ′-rafts inside the band

(b-1) <110>{111} type dislocation entering γ′-phase is selectively enhanced by native dislocations formed during aging treatments

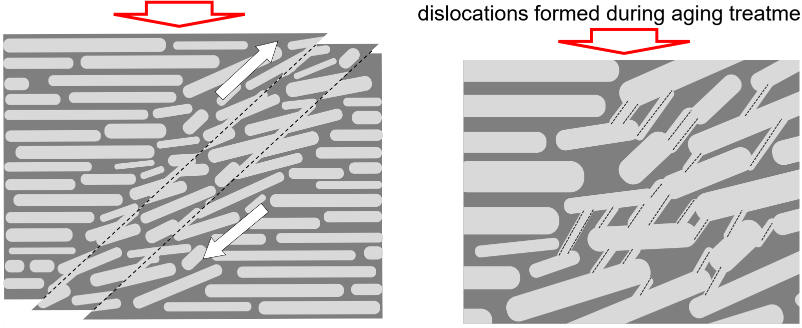

(c) Intense shearing within the band creates plane with very high dislocation density, assisting segregation of solute elements and creates long and connected structure

(b-2) Solute element segregation in shearing dislocations assists γ-phase to grow into long and connected structure parallel to the band

Figure 22. Schematic illustration of creep damage localization processes. (a) Completion of γ'-raft during a creep deformation. (b) higher temperature-lower stress creep conditions where dislocation entering γ' promotes microstructure evolution. (c) higher stress creep situation that localized sharing of whole microstructure dominates the damaging.

4.4. Effect of alloy composition

While creep life reductions of pre-deformed SX superalloys AM1 at 1050 °C, AM1 at 950 °C and CMSX-4 Plus at 1150 °C were similar in terms of life reduction and planar fracture with recrystallized slip plane, CMSX-4 Plus performed differently at temperatures below 1050 °C. The reasons for CMSX-4 Plus being more tolerant to pre-deformation can be discussed from the dislocation structure and precipitate evolution analyses of this study.

We have discussed that AM1 stored higher magnitude of energy within one deformation band, and this caused precipitate evolution with higher tendency of directional coarsening compared to CMSX-4 Plus. Dislocation structures inside the microstructure coarsened bands were more complex and denser in the case of AM1. As a consequence, shearing enhancing effect within the microstructure coarsened band could occur much easier in AM1 than in CMSX-4 Plus. This is a reason why creep life reduction with localized failure process was observed for AM1 regardless of creep conditions.

Solute segregation from **Figs. 12** and **15** can also support the observed differences in creep performances at lower temperatures below topological inversion regime (i.e. γ' volume fraction >50%). Particularly the presence of Re in CMSX-4 Plus and Re segregation at dislocations in **Fig. 15(c)** is one important difference between the two alloys. The Re effect associated with the segregation at dislocations [60,96,97] is often discussed as a factor retarding creep deformation since slower diffusion of Re compared to the other alloying element limits the overall diffusion rate [98–100]. EBSD analysis in **Fig. 17(b)** showed that creep damage localization at the band is not necessarily related to creep void nucleation and crack propagation at 1050 °C for CMSX-4 Plus. Moreover, the γ/γ′ microstructure shown in **Fig. 21(b)** does not present strong inclination of γ′-rafts at the microstructure coarsened band. This suggests that the topological inversion process is erasing all the prior microstructure degradation rapidly in terms of precipitate morphologies. Therefore, the further creep resistance after the topological inversion is controlled by 1) diffusivity and 2) magnitude of plastic activities leading to native dislocation density before the creep tests.

If the Re strengthening is active for CMSX-4 Plus, the question is why it is not effective at 1150 °C. This question helps to understand the most critical situation when the pre-deformation decreases the creep life of a Ni-based SX superalloy. The rafting regime (γ′ volume fraction ≤50%) for AM1 is around 1050 °C and for CMSX-4 Plus is 1150 °C [32]. At the rafting regime, creep deformation rate is limited by the distance which dislocation needs to by-pass through γ/γ′ interface and then the penetration of γ′ phase. If the diffusion is fast enough that by-passing dislocation is not limited by the solute dragging, kinetics of whole process is accelerated by the coarse and inclined microstructure, and hence the creep life degradation mechanism works similarly regardless of composition or the size of microstructure coarsened band.

5. CONCLUSIONS

Minor prior plastic strain (~0.8%) was introduced at room temperature into the as-solutioned Ni-based single crystal superalloys AM1 and CMSX-4 Plus followed by aging heat treatments. This study was designed to mimic the pre-deformation of a turbine blade material that can be introduced during the processing. Associated microstructural changes were analyzed and characterized at different length scales to understand the microstructure evolution behavior and mechanisms leading to damage localization during high temperature creep deformation. The following conclusions can be made from the present study.

- Dislocation climb is the main mechanism of dislocation and microstructure evolution during aging treatment after the pre-deformation of as-solutioned Ni-based SX superalloys. This mainly occurs during the first stage of aging treatment at 1100 °C for AM1 and 1165 °C for CMSX-4 Plus. The process is similar to that occurring at the beginning of primary creep stage in high-temperature low-stress "γ′-rafting regime" creep.

- The effect of pre-deformation on γ′ precipitate size and shape of CMSX-4 Plus is minor compared to that of AM1 that presented γ′-rafting type coarsening. Higher γ/γ′ lattice misfit of AM1 at HT temperature and lower stored strain energy in a single pre-deformation slip band of CMSX-4 Plus is probably a reason for less affected microstructure.

- TEM observations revealed that dislocations are already shearing into γ′ phase during the heat treatment with local γ-former solute segregations at the shearing dislocations. After high temperature creep on pre-deformed CMSX-4 Plus, intense creep damage localization by dislocation shearing into γ′ phase at the microstructure coarsened bands were observed using ECCI in SEM. "Ready-to-shear" γ′ dislocations already existing before the creep test are the origin of creep damage localization.

- Creep properties of CMSX-4 Plus were not affected significantly at temperatures lower than 1050 °C, whereas AM1 has creep life reduction for all creep conditions reported in our previous study [25]. Pre-deformation induced dislocations are contributing to the acceleration of creep damage accumulation differently depending on the creep conditions. At the temperature above the γ′-rafting regime (γ′ volume fraction ≤50%), coarse and inclined γ′-

rafting microstructure formation accelerates kinetics of local creep damage accumulation regardless of alloy chemistry. At the lower temperatures below topological inversion regime (i.e. γ' volume fraction >50%), diffusivity and native dislocation structure are playing role, and hence, CMSX-4 Plus with high Re content is hardly affected by the pre-deformation.

Acknowledgement

Safran Aircraft Engines is acknowledged for its financial support, for providing material, and for their continuous interest in the subject. Sandrine Charles, and Dr. Elodie Drouelle (Safran Aircraft Engines) are gratefully acknowledged for their suggestions and discussions. Institut Pprime gratefully acknowledges “Contrat de Plan Etat - Région Nouvelle-Aquitaine (CPER)” as well as the “Fonds Européen de Développement Régional (FEDER)” for their financial support to the reported work. Scanning transmission electron microscopy was performed at the Center for Electron Microscopy and Analysis (CEMAS) at The Ohio State University. Authors would like to thank Dr. Veronika Mazánová (IPM, CAS) for help with the production of 3D anaglyphs and Dagmar Herzánová (IPM, CAS) for the preparation of twin-jet electropolished disc foils.

References

[1] R.C. Reed, The Superalloys: Fundamentals and Applications, Cambridge University Press, Cambridge, 2006. https://doi.org/10.1017/CBO9780511541285.

[2] T.M. Pollock, S. Tin, Nickel-Based Superalloys for Advanced Turbine Engines: Chemistry, Microstructure and Properties, J. Propuls. Power 22 (2006) 361–374. https://doi.org/10.2514/1.18239.

[3] H. Long, S. Mao, Y. Liu, Z. Zhang, X. Han, Microstructural and compositional design of Ni-based single crystalline superalloys — A review, J. Alloys Compd. 743 (2018) 203–220. https://doi.org/10.1016/j.jallcom.2018.01.224.

[4] M.V. Nathal, Effect of initial gamma prime size on the elevated temperature creep properties of single crystal nickel base superalloys, Metall. Trans. A 18 (1987) 1961–1970. https://doi.org/10.1007/BF02647026.

[5] A. Sengupta, S.K. Putatunda, L. Bartosiewicz, J. Hangas, P.J. Nailos, M. Peputapeck, F.E. Alberts, Tensile behavior of a new single-crystal nickel-based superalloy (CMSX-4) at room

and elevated temperatures, J. Mater. Eng. Perform. 3 (1994) 73–81. https://doi.org/10.1007/BF02654502.

[6] P. Caron, P.J. Henderson, T. Khan, M. McLean, On the effects of heat treatments on the creep behaviour of a single crystal superalloy, Scr. Metall. 20 (1986) 875–880. https://doi.org/10.1016/0036-9748(86)90458-8.

[7] S. Pierret, T. Etter, A. Evans, H. Van Swygenhoven, Origin of localized rafting in Ni-based single crystal turbine blades before service and its influence on the mechanical properties, Acta Mater. 61 (2013) 1478–1488. https://doi.org/10.1016/j.actamat.2012.11.024.

[8] K. Park, J. Davies, P. Withey, Microstructural Investigation of Stress-Induced Degradation of Gamma and Gamma Prime Phases on the Surface of the Aerofoil of Nickel-Based Single Crystal Superalloy Turbine Blades, Crystals 15 (2025) 553. https://doi.org/10.3390/cryst15060553.

[9] H.N. Mathur, C. Panwisawas, C.N. Jones, R.C. Reed, C.M.F. Rae, Nucleation of recrystallisation in castings of single crystal Ni-based superalloys, Acta Mater. 129 (2017) 112–123. https://doi.org/10.1016/j.actamat.2017.02.058.

[10] L. Tian, C. Xu, C. Ma, Recrystallization of a single crystal Ni-base superalloy in ⟨011⟩ and ⟨111⟩ orientations, Mater. Charact. 127 (2017) 116–120. https://doi.org/10.1016/j.matchar.2017.01.020.

[11] L. Zhonglin, Z. Dandan, S. Xianglin, X. Qingyan, L. Baicheng, Role of as-cast dendritic microstructure in recrystallization of a Ni-based single crystal superalloy, J. Alloys Compd. 660 (2016) 115–124. https://doi.org/10.1016/j.jallcom.2015.11.072.

[12] F.Z. Xu, Y.C. Lin, D.X. Ma, G.C. Wu, B.W. Cheng, D.G. He, Y.X. Zhao, L. Li, Y.P. Deng, J.H. Wei, Effect of high-temperature stress relief annealing on the recrystallization of pre-deformed Ni-based single crystal superalloy, J. Alloys Compd. 1024 (2025) 180056. https://doi.org/10.1016/j.jallcom.2025.180056.

[13] W. Xiong, Z. Huang, G. Xie, Z. Ge, X. Wang, Y. Lu, W. Zheng, L. Lou, J. Zhang, The effect of deformation temperature on recrystallization in a Ni-based single crystal superalloys, Mater. Des. 222 (2022) 111042. https://doi.org/10.1016/j.matdes.2022.111042.

[14] D.C. Cox, B. Roebuck, C.M.F. Rae, R.C. Reed, Recrystallisation of single crystal superalloy CMSX-4, Mater. Sci. Technol. 19 (2003) 440–446. https://doi.org/10.1179/026708303225010731.

[15] R. Bürgel, P.D. Portella, J. Preuhs, Recrystallization in single crystals of nickel base superalloys, in: Superalloys 2000, 2000: pp. 229–238. https://doi.org/10.7449/2000/Superalloys_2000_229_238.

[16] H. Long, S. Mao, Y. Liu, H. Wei, Q. Deng, Y. Chen, Z. Zhang, X. Han, Effect of pre-straining treatment on high temperature creep behavior of Ni-based single crystal superalloys, Mater. Des. (2019) 107633. https://doi.org/10.1016/j.matdes.2019.107633.

[17] G.L. Drew, R.C. Reed, K. Kakehi, C.M.F. Rae, Single Crystal Superalloys: The transition

from Primary to Secondary Creep, in: Superalloys 2004, 2004: pp. 127–136. https://doi.org/10.7449/2004/Superalloys_2004_127_136.

[18] Y. Su, S. Tian, H. Yu, L. Yu, Effect of pre-compressive treatment on creep behavior of a ⟨011⟩-oriented single-crystal Ni-based superalloy, Scr. Mater. 93 (2014) 24–27. https://doi.org/10.1016/j.scriptamat.2014.08.021.

[19] R. Giraud, J. Cormier, Z. Hervier, D. Bertheau, K. Harris, J. Wahl, X. Milhet, J. Mendez, A. Organista, Effect of the Prior Microstructure Degradation on the High Temperature/Low Stress Non-Isothermal Creep Behavior of CMSX-4® Ni-Based Single Crystal Superalloy, 2012. https://doi.org/10.1002/9781118516430.ch29.

[20] U. Tetzlaff, H. Mughrabi, Enhancement of the high-temperature tensile creep strength of monocrystalline nickel-base superalloys by pre-rafting in compression, in: Superalloys 2000, 2000: pp. 273–282. https://doi.org/10.7449/2000/Superalloys_2000_273_282.

[21] M. Sakaguchi, M. Ike, M. Okazaki, Microstructural changes in a single crystal Ni-base superalloy induced by plastic straining, Mater. Sci. Eng. A 534 (2012) 253–259. https://doi.org/10.1016/J.MSEA.2011.11.066.

[22] M. Sakaguchi, M. Okazaki, Distinctive role of plastic and creep strain in directional coarsening of a Ni-base single crystal superalloy, Mater. Sci. Eng. A 710 (2018) 121–128. https://doi.org/10.1016/j.msea.2017.10.085.

[23] B.G. Choi, C.Y. Jo, H.U. Hong, I.S. Kim, S.M. Seo, H.M. Kim, Effect of pre-strain on microstructural evolution during thermal exposure of single crystal superalloy CMSX-4, Trans. Nonferrous Met. Soc. China 21 (2011) 1291–1296. https://doi.org/10.1016/S1003-6326(11)60855-8.

[24] C.P. Liu, X.N. Zhang, L. Ge, C.Y. Wang, T. Yu, Z. Zhang, The effect of pre-deformation on the microstructure evolution of NiAl model single crystal superalloy during thermal exposure at 1000 °C, Mater. Sci. Eng. A 754 (2019) 556–561. https://doi.org/10.1016/j.msea.2019.03.099.

[25] S. Hamadi, F. Hamon, J. Delautre, J. Cormier, P. Villechaise, S. Utada, P. Kontis, N. Bozzolo, Consequences of a Room-Temperature Plastic Deformation During Processing on Creep Durability of a Ni-Based SX Superalloy, Metall. Mater. Trans. A 49 (2018) 4246–4261. https://doi.org/10.1007/s11661-018-4748-3.

[26] S. Utada, J. Rame, S. Hamadi, J. Delautre, P. Villechaise, J. Cormier, Kinetics of creep damage accumulation induced by a room-temperature plastic deformation introduced during processing of AM1 Ni-based single crystal superalloy, Mater. Sci. Eng. A 789 (2020) 139571. https://doi.org/10.1016/j.msea.2020.139571.

[27] S. Utada, J. Rame, S. Hamadi, J. Delautre, L. Mataveli Suave, P. Villechaise, J. Cormier, High-temperature pre-deformation and rejuvenation treatment on the microstructure and creep properties of Ni-based single crystal superalloys, in: S. Tin, M. Hardy, J. Clews, J. Cormier, Q. Feng, J. Marcin, C. O'Brien, A. Suzuki (Eds.), Superalloys 2020, Springer International

Publishing, 2020: pp. 240–252. https://doi.org/10.1007/978-3-030-51834-9_23.

[28] A. Epishin, T. Link, Mechanisms of high-temperature creep of nickel-based superalloys under low applied stresses, Philos. Mag. 84 (2004) 1979–2000. https://doi.org/10.1080/14786430410001663240.

[29] T. Link, S. Zabler, A. Epishin, A. Haibel, M. Bansal, X. Thibault, Synchrotron tomography of porosity in single-crystal nickel-base superalloys, Mater. Sci. Eng. A 425 (2006) 47–54. https://doi.org/10.1016/j.msea.2006.03.005.

[30] J.B. Wahl, K. Harris, CMSX-4 Plus Single Crystal Alloy Development, Characterization and Application Development, in: Superalloys 2016, John Wiley & Sons, Inc., 2016: pp. 25–33. https://doi.org/10.1002/9781119075646.ch3.

[31] J. Cormier, Thermal Cycling Creep Resistance of Ni-Based Single Crystal Superalloys, in: Superalloys 2016, John Wiley & Sons, Inc., 2016: pp. 383–394. https://doi.org/doi:10.1002/9781119075646.ch42.

[32] S. Utada, L. Després, J. Cormier, Ultra-High Temperature Creep of Ni-Based SX Superalloys at 1250 °C, Metals 11 (2021) 1610. https://doi.org/10.3390/met11101610.

[33] F. Hanriot, G. Cailletaud, L. Remy, Mechanical behavior of a nickel-base superalloy single crystal, in: Winter Annu. Meet. Am. Soc. Mech. Eng., ASME, Atlanta, GA, USA, 1991: pp. 139–150.

[34] J.H. Davidson, A. Fredholm, T. Khan, J.-M.C.F. Theret, Single-crystal alloy has a nickel base matrix, 1986. https://patents.google.com/patent/FR2557598B1/en.

[35] J. Cormier, M. Jouiad, F. Hamon, P. Villechaise, X. Milhet, Very high temperature creep behavior of a single crystal Ni-based superalloy under complex thermal cycling conditions, Philos. Mag. Lett. 90 (2010) 611–620. https://doi.org/10.1080/09500839.2010.489887.

[36] V. Caccuri, J. Cormier, R. Desmorat, γ′-Rafting mechanisms under complex mechanical stress state in Ni-based single crystalline superalloys, Mater. Des. 131 (2017) 487–497. https://doi.org/10.1016/j.matdes.2017.06.018.

[37] V. Caccuri, R. Desmorat, J. Cormier, Tensorial nature of γ′-rafting evolution in nickel-based single crystal superalloys, Acta Mater. 158 (2018) 138–154. https://doi.org/10.1016/j.actamat.2018.07.033.

[38] P.J. Phillips, M.C. Brandes, M.J. Mills, M. De Graef, Diffraction contrast STEM of dislocations: Imaging and simulations, Ultramicroscopy 111 (2011) 1483–1487. https://doi.org/10.1016/j.ultramic.2011.07.001.

[39] M. Heczko, B.D. Esser, T.M. Smith, P. Beran, V. Mazánová, D.W. McComb, T. Kruml, J. Polák, M.J. Mills, Atomic resolution characterization of strengthening nanoparticles in a new high-temperature-capable 43Fe-25Ni-22.5Cr austenitic stainless steel, Mater. Sci. Eng. A 719 (2018) 49–60. https://doi.org/10.1016/j.msea.2018.02.004.

[40] A. Dlouhý, J. Pešička, Estimate of foil thickness by stereomicroscopy technique, Czechoslov. J. Phys. 40 (1990) 539–555. https://doi.org/10.1007/BF01599778.

[41] L. Agudo Jácome, G. Eggeler, A. Dlouhý, Advanced scanning transmission stereo electron microscopy of structural and functional engineering materials, Ultramicroscopy 122 (2012) 48–59. https://doi.org/10.1016/j.ultramic.2012.06.017.

[42] T. Sekitani, Anaglyph Maker Ver1.08, STEREOeYe (2001). https://www.stereoeye.jp/software/index_e.html (accessed December 13, 2024).

[43] L.M. Bortoluci Ormastroni, S. Utada, J. Rame, L. Mataveli Suave, K. Kawagishi, H. Harada, P. Villechaise, J. Cormier, Tensile, low cycle fatigue and very high cycle fatigue characterizations of advanced single crystal nickel-based superalloys, in: S. Tin, M. Hardy, J. Clews, J. Cormier, Q. Feng, J. Marcin, C. O'Brien, A. Suzuki (Eds.), Superalloys 2020, Springer International Publishing, 2020: pp. 341–351. https://doi.org/10.1007/978-3-030-51834-9_33.

[44] B. Mansoz, L.M. Bortoluci Ormastroni, J. Rame, C. Schwalbe, K.V. Vamsi, P. Caron, J. Cormier, F. Pettinari-Sturmel, Tensile behavior of single crystal nickel-based superalloys at 650°C, Intermetallics 161 (2023) 107976. https://doi.org/10.1016/j.intermet.2023.107976.

[45] K.V. Vamsi, S. Karthikeyan, Modeling APB energies in multicomponent Ni-base superalloys, Intermetallics 132 (2021) 107124. https://doi.org/10.1016/j.intermet.2021.107124.

[46] P. Beardmore, R.G. Davies, T.L. Johnston, On the Temperature Dependence of the Flow Stress of Nickel-Base Alloys, Trans. Metall. Soc. AlME 245 (1969) 1537–1545.

[47] D.M. Shah, D.N. Duhl, The effect of orientation, temperature and gamma prime size on the yield strength of a single crystal nickel base superalloy, Superalloys 1984 (1984) 105–114.

[48] M. Kamaraj, Rafting in single crystal nickel-base superalloys — An overview, Sadhana 28 (2003) 115–128. https://doi.org/10.1007/BF02717129.

[49] A.B. Parsa, P. Wollgramm, H. Buck, A. Kostka, C. Somsen, A. Dlouhy, G. Eggeler, Ledges and grooves at γ/γ′ interfaces of single crystal superalloys, Acta Mater. 90 (2015) 105–117. https://doi.org/10.1016/j.actamat.2015.02.005.

[50] M. Kolbe, A. Dlouhy, G. Eggeler, Dislocation reactions at γ/γ′-interfaces during shear creep deformation in the macroscopic crystallographic shear system (001)[110] of CMSX6 superalloy single crystals at 1025°C, Mater. Sci. Eng. A 246 (1998) 133–142. https://doi.org/10.1016/S0921-5093(97)00733-8.

[51] G. Eggeler, A. Dlouhy, On the formation of 〈010〉-dislocations in the γ′-phase of superalloy single crystals during high temperature low stress creep, Acta Mater. 45 (1997) 4251–4262. https://doi.org/10.1016/S1359-6454(97)00084-0.

[52] H. Long, H. Wei, Y. Liu, S. Mao, J. Zhang, S. Xiang, Y. Chen, W. Gui, Q. Li, Z. Zhang, X. Han, Effect of lattice misfit on the evolution of the dislocation structure in Ni-based single crystal superalloys during thermal exposure, Acta Mater. 120 (2016) 95–107. https://doi.org/10.1016/j.actamat.2016.08.035.

[53] J. Zhang, J. Wang, H. Harada, Y. Koizumi, The effect of lattice misfit on the dislocation motion in superalloys during high-temperature low-stress creep, Acta Mater. 53 (2005) 4623–4633. https://doi.org/10.1016/j.actamat.2005.06.013.

[54] T. Link, A. Epishin, M. Paulisch, T. May, Topography of semicoherent γ/γ′-interfaces in superalloys: Investigation of the formation mechanism, Mater. Sci. Eng. A 528 (2011) 6225–6234. https://doi.org/10.1016/j.msea.2011.04.049.

[55] A. Epishin, T. Link, G. Nolze, SEM investigation of interfacial dislocations in nickel-base superalloys, J. Microsc. 228 (2007) 110–117. https://doi.org/10.1111/j.1365-2818.2007.01831.x.

[56] D. Qi, L. Wang, P. Zhao, L. Qi, S. He, Y. Qi, H. Ye, J. Zhang, K. Du, Facilitating effect of interfacial grooves on the rafting of nickel-based single crystal superalloy at high temperature, Scr. Mater. 167 (2019) 71–75. https://doi.org/10.1016/j.scriptamat.2019.04.001.

[57] P. Kontis, Z. Li, D.M. Collins, J. Cormier, D. Raabe, B. Gault, The effect of chromium and cobalt segregation at dislocations on nickel-based superalloys, Scr. Mater. 145 (2018) 76–80. https://doi.org/10.1016/j.scriptamat.2017.10.005.

[58] S. Antonov, Y. Zheng, J.M. Sosa, H.L. Fraser, J. Cormier, P. Kontis, B. Gault, Plasticity assisted redistribution of solutes leading to topological inversion during creep of superalloys, Scr. Mater. 186 (2020) 287–292. https://doi.org/10.1016/j.scriptamat.2020.05.004.

[59] P. Kontis, T.M. Smith, A Review on the Partitioning of Solutes Along Dislocations and Stacking Faults in Superalloys, Metall. Mater. Trans. A 55 (2024) 4723–4741. https://doi.org/10.1007/s11661-024-07626-y.

[60] A. Cervellon, S. Hémery, P. Kürnsteiner, B. Gault, P. Kontis, J. Cormier, Crack initiation mechanisms during very high cycle fatigue of Ni-based single crystal superalloys at high temperature, Acta Mater. 188 (2020) 131–144. https://doi.org/10.1016/j.actamat.2020.02.012.

[61] J. Zhang, F. Lu, T. Huang, R. Li, G. Zhang, L. Liu, An advanced approach to improve the high-temperature property for Ni-based superalloys: Interface segregation manipulation, Mater. Sci. Eng. A 881 (2023) 145382. https://doi.org/10.1016/j.msea.2023.145382.

[62] J. Sun, J. Liu, C. Chen, J. Li, X. Wang, X. Sun, Effect of Ru on γ/γ’ microstructural evolutions and precipitation of TCP phases during thermal exposure at 1100 °C in a single crystal superalloy, Mater. Charact. 186 (2022) 111794. https://doi.org/10.1016/j.matchar.2022.111794.

[63] J.X. Zhang, H. Harada, Y. Koizumi, T. Kobayashi, Dislocation motion in the early stages of high-temperature low-stress creep in a single-crystal superalloy with a small lattice misfit, J. Mater. Sci. 45 (2010) 523–532. https://doi.org/10.1007/s10853-009-3970-1.

[64] N. Matan, D.C. Cox, C.M.F. Rae, R.C. Reed, On the kinetics of rafting in CMSX-4 superalloy single crystals, Acta Mater. 47 (1999) 2031–2045. https://doi.org/10.1016/S1359-6454(99)00093-2.

[65] A. Lasalmonie, J.L. Strudel, Interfacial dislocation networks around γ′ precipitates in

nickel-base alloys, Philos. Mag. J. Theor. Exp. Appl. Phys. 32 (1975) 937–949. https://doi.org/10.1080/14786437508221665.

[66] T. Sugui, Z. Huihua, Z. Jinghua, Y. Hongcai, X. Yongbo, H. Zhuangqi, Formation and role of dislocation networks during high temperature creep of a single crystal nickel–base superalloy, Mater. Sci. Eng. A 279 (2000) 160–165. https://doi.org/10.1016/S0921-5093(99)00623-1.

[67] L.J. Carroll, Q. Feng, T.M. Pollock, Interfacial Dislocation Networks and Creep in Directional Coarsened Ru-Containing Nickel-Base Single-Crystal Superalloys, Metall. Mater. Trans. A 39 (2008) 1290–1307. https://doi.org/10.1007/s11661-008-9520-7.

[68] A.K. Singh, N. Louat, K. Sadananda, Dislocation network formation and coherency loss around gamma- prime precipitates in a nickel- base superalloy, Metall. Trans. A 19 (1988) 2965–2973. https://doi.org/10.1007/BF02647723.

[69] A. Royer, P. Bastie, D. Bellet, J.L. Strudel, Temperature dependence of the lattice mismatch of the AM1 superalloy influence of the γ′ precipitates’ morphology, Philos. Mag. A 72 (1995) 669–689. https://doi.org/10.1080/01418619508243792.

[70] L. Dirand, J. Cormier, A. Jacques, J.-P. Chateau-Cornu, T. Schenk, O. Ferry, P. Bastie, Measurement of the effective γ/γ′ lattice mismatch during high temperature creep of Ni-based single crystal superalloy, Mater. Charact. 77 (2013) 32–46. https://doi.org/10.1016/J.MATCHAR.2012.12.003.

[71] T. Yamagata, H. Harada, S. Nakazawa, M. Yamazaki, Y.G. Nakagawa, Alloy Design for high Strangth Ni-base Single Crystal Alloys, in: Superalloys 1984, 1984: pp. 157–166.

[72] T. Yokokawa, H. Harada, K. Kawagishi, T. Kobayashi, M. Yuyama, Y. Takata, Advanced Alloy Design Program and Improvement of Sixth-Generation Ni-Base Single Crystal Superalloy TMS-238, in: S. Tin, M. Hardy, J. Clews, J. Cormier, Q. Feng, J. Marcin, C. O’Brien, A. Suzuki (Eds.), Superalloys 2020, Springer International Publishing, Cham, 2020: pp. 122–130. https://doi.org/10.1007/978-3-030-51834-9_12.

[73] H. Harada, H. Murakami, Design of Ni-Base Superalloys, in: T. Saito (Ed.), Comput. Mater. Des., Springer Berlin Heidelberg, Berlin, Heidelberg, 1999: pp. 39–70. https://doi.org/10.1007/978-3-662-03923-6_2.

[74] S. Huang, K. An, Y. Gao, A. Suzuki, Determination of γ/γ′ Lattice Misfit in Ni-Based Single-Crystal Superalloys at High Temperatures by Neutron Diffraction, Metall. Mater. Trans. A 49 (2018) 740–751. https://doi.org/10.1007/s11661-017-4455-5.

[75] L. Agudo Jácome, P. Nörtershäuser, C. Somsen, A. Dlouhý, G. Eggeler, On the nature of γ′ phase cutting and its effect on high temperature and low stress creep anisotropy of Ni-base single crystal superalloys, Acta Mater. 69 (2014) 246–264. https://doi.org/10.1016/j.actamat.2014.01.021.

[76] A.B. Parsa, D. Bürger, T.M. Pollock, G. Eggeler, Misfit and the mechanism of high temperature and low stress creep of Ni-base single crystal superalloys, Acta Mater. 264 (2024)

119576. https://doi.org/10.1016/j.actamat.2023.119576.

[77] P.M. Sarosi, R. Srinivasan, G.F. Eggeler, M.V. Nathal, M.J. Mills, Observations of a ⟨010⟩ dislocations during the high-temperature creep of Ni-based superalloy single crystals deformed along the [001] orientation, Acta Mater. 55 (2007) 2509–2518. https://doi.org/10.1016/j.actamat.2006.11.045.

[78] A.-C. Yeh, A. Sato, T. Kobayashi, H. Harada, On the creep and phase stability of advanced Ni-base single crystal superalloys, Mater. Sci. Eng. A 490 (2008) 445–451. https://doi.org/10.1016/j.msea.2008.02.008.

[79] T.M. Pollock, A.S. Argon, Creep resistance of CMSX-3 nickel base superalloy single crystals, Acta Metall. Mater. 40 (1992) 1–30. https://doi.org/10.1016/0956-7151(92)90195-K.

[80] A.I. Epishin, I.L. Svetlov, Evolution of pore morphology in single-crystals of nickel-base superalloys, Inorg. Mater. Appl. Res. 7 (2016) 45–52. https://doi.org/10.1134/S2075113316010056.

[81] J.-B. le Graverend, J. Adrien, J. Cormier, Ex-situ X-ray tomography characterization of porosity during high-temperature creep in a Ni-based single-crystal superalloy: Toward understanding what is damage, Mater. Sci. Eng. A 695 (2017) 367–378. https://doi.org/10.1016/j.msea.2017.03.083.

[82] R.C. Reed, D.C. Cox, C.M.F. Rae, Damage accumulation during creep deformation of a single crystal superalloy at 1150 °C, Mater. Sci. Eng. A 448 (2007) 88–96. https://doi.org/10.1016/J.MSEA.2006.11.101.

[83] S.H. Ai, V. Lupinc, M. Maldini, Creep fracture mechanisms in single crystal superalloys, Scr. Metall. Mater. 26 (1992) 579–584. https://doi.org/10.1016/0956-716X(92)90287-O.

[84] X.G. Wang, J.L. Liu, T. Jin, X.F. Sun, Y.Z. Zhou, Z.Q. Hu, J.H. Do, B.G. Choi, I.S. Kim, C.Y. Jo, Creep deformation related to dislocations cutting the γ′ phase of a Ni-base single crystal superalloy, Mater. Sci. Eng. A 626 (2015) 406–414. https://doi.org/10.1016/j.msea.2014.12.060.

[85] C.M.F. Rae, M.A. Rist, D.C. Cox, R.C. Reed, N. Matan, On the primary creep of CMSX-4 superalloy single crystals, Metall. Mater. Trans. A 31 (2000) 2219–2228. https://doi.org/10.1007/s11661-000-0139-6.

[86] J.X. Zhang, T. Murakumo, Y. Koizumi, T. Kobayashi, H. Harada, Slip geometry of dislocations related to cutting of the γ′ phase in a new generation single-crystal superalloy, Acta Mater. 51 (2003) 5073–5081. https://doi.org/10.1016/S1359-6454(03)00355-0.

[87] R. Srinivasan, G.F. Eggeler, M.J. Mills, γ′-cutting as rate-controlling recovery process during high-temperature and low-stress creep of superalloy single crystals, Acta Mater. 48 (2000) 4867–4878. https://doi.org/10.1016/S1359-6454(00)00292-5.

[88] A. Epishin, T. Link, U. Brückner, P.D. Portella, Kinetics of the topological inversion of the γ/γ′-microstructure during creep of a nickel-based superalloy, Acta Mater. 49 (2001) 4017–

4023. https://doi.org/10.1016/S1359-6454(01)00290-7.

[89] P. Caron, C. Ramusat, F. Diologent, Influence of the γ′ fraction on the γ/γ′ topological inversion during high temperature creep of single crystal superalloys, in: Superalloys 2008, TMS Warrendale, PA, 2008: pp. 159–167. https://doi.org/10.7449/2008/Superalloys_2008_159_167.

[90] M. Legros, N. Clément, P. Caron, A. Coujou, In-situ observation of deformation micromechanisms in a rafted γ/γ′ superalloy at 850°C, Mater. Sci. Eng. A 337 (2002) 160–169. https://doi.org/10.1016/S0921-5093(02)00037-0.

[91] X. Wu, A. Dlouhy, Y.M. Eggeler, E. Spiecker, A. Kostka, C. Somsen, G. Eggeler, On the nucleation of planar faults during low temperature and high stress creep of single crystal Ni-base superalloys, Acta Mater. 144 (2018) 642–655. https://doi.org/10.1016/j.actamat.2017.09.063.

[92] J. He, C.H. Zenk, X. Zhou, S. Neumeier, D. Raabe, B. Gault, S.K. Makineni, On the atomic solute diffusional mechanisms during compressive creep deformation of a Co-Al-W-Ta single crystal superalloy, Acta Mater. 184 (2020) 86–99. https://doi.org/10.1016/j.actamat.2019.11.035.

[93] S. Utada, L.M. Bortoluci Ormastroni, J. Rame, P. Villechaise, J. Cormier, VHCF life of AM1 Ni-based single crystal superalloy after pre-deformation, Int. J. Fatigue 148 (2021) 106224. https://doi.org/10.1016/j.ijfatigue.2021.106224.

[94] H. Buck, P. Wollgramm, A.B. Parsa, G. Eggeler, A quantitative metallographic assessment of the evolution of porosity during processing and creep in single crystal Ni-base super alloys, Mater. Werkst. 46 (2015) 577–590. https://doi.org/10.1002/mawe.201500379.

[95] A. Epishin, T. Link, I.L. Svetlov, G. Nolze, R.S. Neumann, H. Lucas, Mechanism of porosity growth during homogenisation in single crystal nickel-based superalloys, Int. J. Mater. Res. 104 (2013) 776–782. https://doi.org/10.3139/146.110924.

[96] X. Wu, S.K. Makineni, C.H. Liebscher, G. Dehm, J. Rezaei Mianroodi, P. Shanthraj, B. Svendsen, D. Bürger, G. Eggeler, D. Raabe, B. Gault, Unveiling the Re effect in Ni-based single crystal superalloys, Nat. Commun. 11 (2020) 389. https://doi.org/10.1038/s41467-019-14062-9.

[97] X. Wu, S.K. Makineni, P. Kontis, G. Dehm, D. Raabe, B. Gault, G. Eggeler, On the segregation of Re at dislocations in the γ’ phase of Ni-based single crystal superalloys, Materialia 4 (2018) 109–114. https://doi.org/10.1016/j.mtla.2018.09.018.

[98] A.F. Giamei, D.L. Anton, Rhenium additions to a Ni-base superalloy: Effects on microstructure, Metall. Trans. A 16 (1985) 1997–2005. https://doi.org/10.1007/BF02662400.

[99] W.Z. Wang, T. Jin, J.L. Liu, X.F. Sun, H.R. Guan, Z.Q. Hu, Role of Re and Co on microstructures and γ′ coarsening in single crystal superalloys, Mater. Sci. Eng. A 479 (2008) 148–156. https://doi.org/10.1016/j.msea.2007.06.031.

[100] M.S.A. Karunaratne, P. Carter, R.C. Reed, Interdiffusion in the face-centred cubic phase

of the Ni-Re, Ni-Ta and Ni-W systems between 900 and 1300°C, Mater. Sci. Eng. A 281 (2000) 229–233.